

# Detecting rapid lateral changes of upper mantle discontinuities using azimuth-dependent P-wave receiver functions and multimode surface waves

K. Tarumi<sup>1,\*</sup> and K. Yoshizawa<sup>1,2</sup>

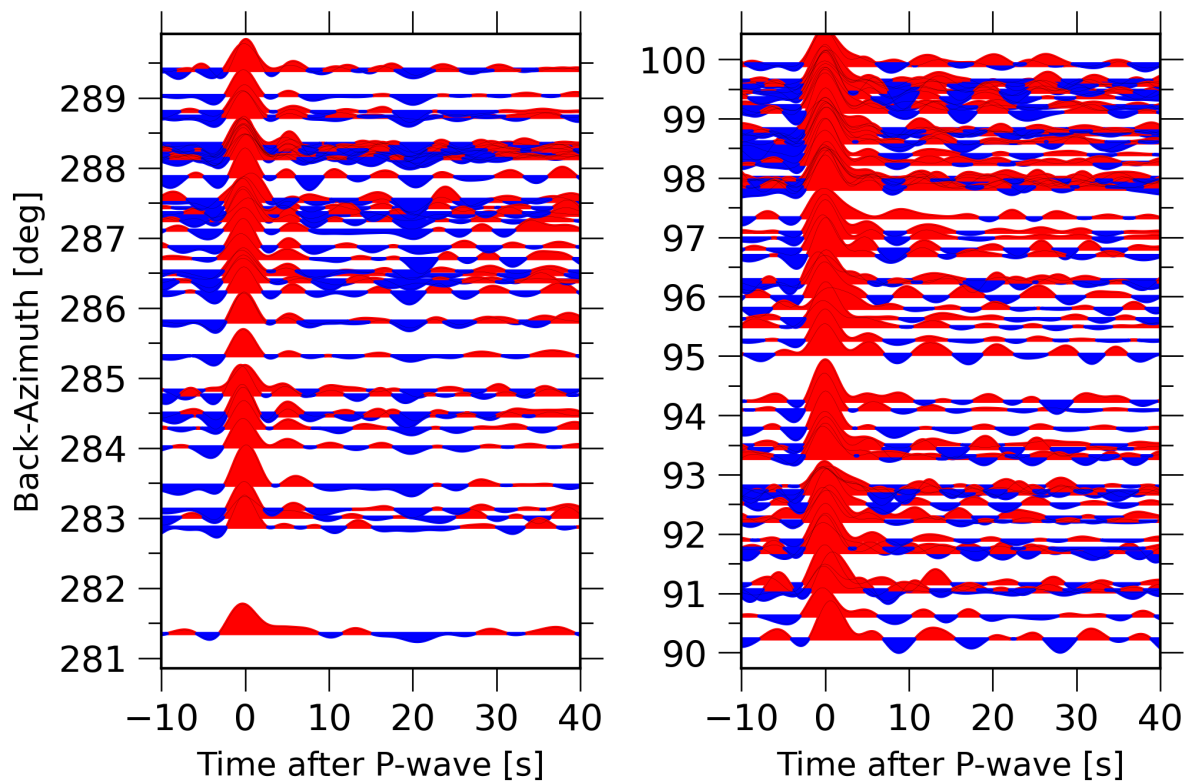
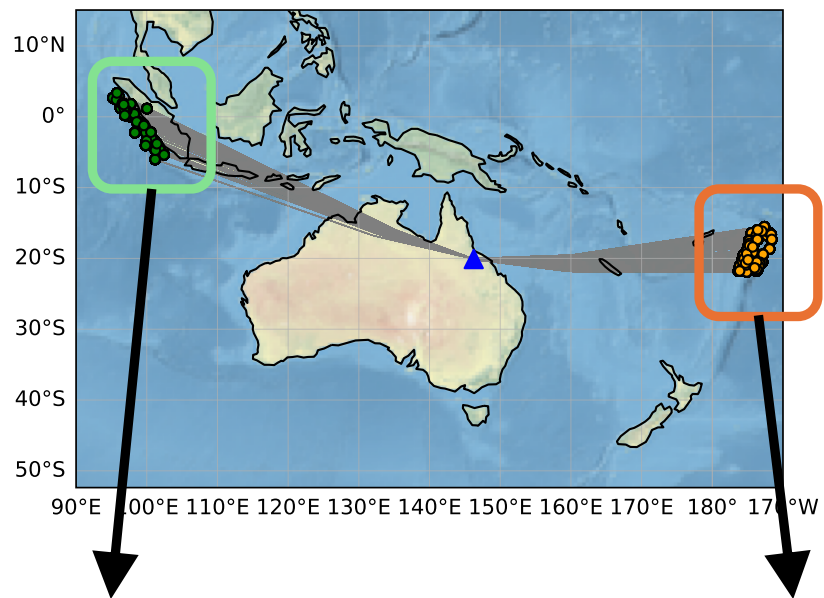
<sup>1</sup> Department of Natural History Sciences, Graduate School of Science, Hokkaido University, Sapporo 060-0810, Japan

<sup>2</sup> Department of Earth & Planetary Sciences, Faculty of Science, Hokkaido University, Sapporo 060-0810, Japan.

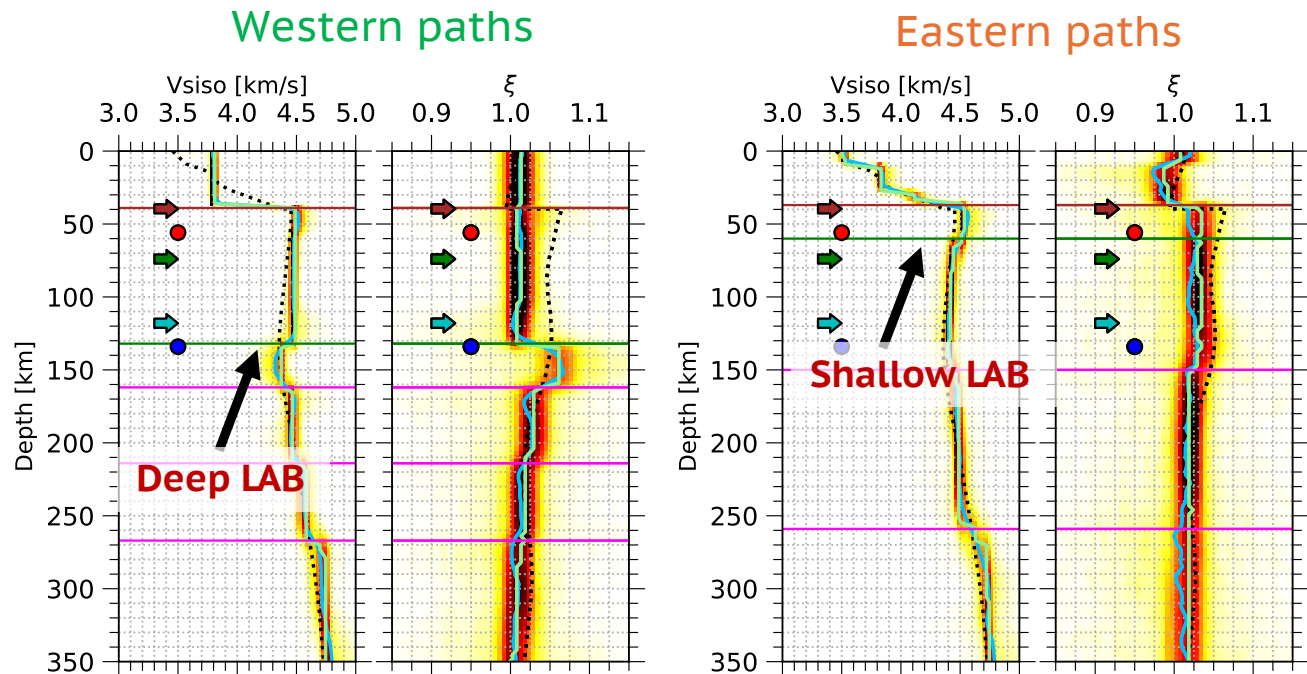
\*Corresponding author: tarumi.kotaro.jp@gmail.com

This is a preprint that is submitted to EarthArXiv. The original manuscript has been submitted to *Physics of the Earth and Planetary Interiors*.

# Azimuth-dependent receiver functions

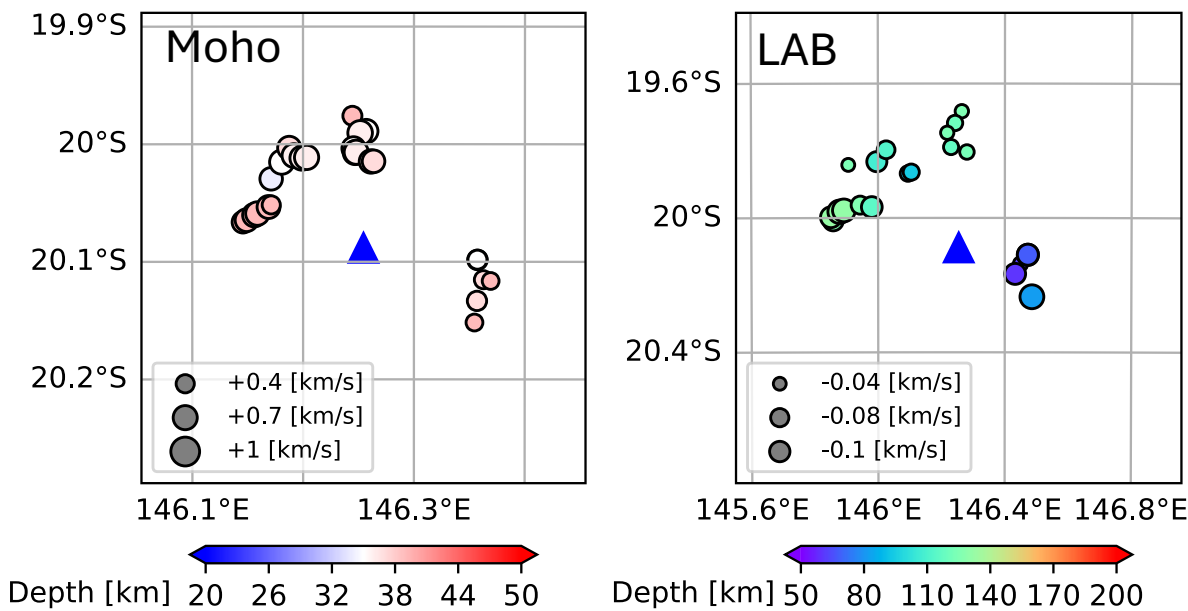


# Results of joint Bayesian inversions of RF and SW



*Compiling estimated discontinuities*

# Ps conversion point maps for seismic discontinuities



# 1 Highlights

## 2 **Detecting rapid lateral changes of upper mantle discontinuities using azimuth-dependent P-** 3 **wave receiver functions and multimode surface waves**

4 Kotaro Tarumi, Kazunori Yoshizawa

- 5 • Azimuth-dependent receiver functions detect lateral changes in seismic interfaces
- 6 • Lithosphere-Asthenosphere Boundary (LAB) rapidly thickens westward in NE Australia
- 7 • Mid-Lithospheric Discontinuity (MLD) beneath cratons comprises multiple interfaces
- 8 • MLDs indicate various characteristics depending on the cratonic blocks
- 9 • Multiple interfaces exist below LAB with velocity jump and weakened radial anisotropy

# Detecting rapid lateral changes of upper mantle discontinuities using azimuth-dependent P-wave receiver functions and multimode surface waves

Kotaro Tarumi<sup>a,\*</sup>, Kazunori Yoshizawa<sup>a,b</sup>

<sup>a</sup>Department of Natural History Sciences, Graduate School of Science, Hokkaido University, Sapporo 060-0810, Japan., Sapporo, 060-0810, Japan

<sup>b</sup>Department of Earth and Planetary Sciences, Faculty of Science, Hokkaido University, Sapporo, 060-0810, Japan

## ARTICLE INFO

### Keywords:

Receiver function

Surface waves

Australia

Lithosphere-Asthenosphere Boundary

Mid-Lithospheric Discontinuity

X-Discontinuity

## ABSTRACT

Lateral structural variations in the upper mantle generate azimuthal dependence in receiver functions (RFs) based on incoming directions of body waves. Although these azimuthal variations in RFs have not been considered in earlier studies of RF inversions, they provide a means to image localized changes in upper mantle interfaces. In this study, we incorporate azimuth-dependent RFs into a joint Bayesian inversion with multimode surface waves, applying this approach to major permanent broadband stations in Australia. The resulting models reveal dependence on event directions, and by identifying P-to-S conversion depths, we constructed a localized map of conversion points, reflecting local lateral variations of upper mantle discontinuities beneath each station. At the CTAO station in northeastern Australia, the lithosphere thickens rapidly northwestward, from 70 km to 120-130 km depth, corresponding to the tectonic boundary with the western cratonic region. At stations in western and central Australia, lithospheric thickness also varies laterally within the stable cratons, though these changes are more gradual than those in northeastern Australia. In addition to the lithosphere-asthenosphere boundary (LAB), both mid-lithospheric discontinuities (MLDs) and X-discontinuities (X-Ds) are observed in the local 1-D profiles. The X-Ds, characterized by seismic velocity jumps below the LAB, are found at multiple depths around 170, 220, 260, and 310 km, depending on location, accompanying the weakened radial anisotropy across these depths. The multiple MLDs are also identified in the cratonic regions, showing substantial variations in their seismological properties, including both positive or negative S-velocity jumps, which vary with location and depth. Our approach, incorporating azimuth-dependent RFs, enables the detection of localized changes in the upper mantle discontinuities and associated elastic properties, providing new insights into the complex layering of the upper mantle.

## 1. Introduction

Upper mantle discontinuities are key to understanding the evolutionary processes of the continental lithosphere and underlying asthenosphere. Seismic interfaces within the continental upper mantle are essential for clarifying the tectonic processes that long-lived continents have undergone. Although these seismic discontinuities have been extensively investigated in various seismological studies, their spatial distributions and elastic properties remain controversial, even in continental regions with extensive seismic networks (e.g., Fischer et al., 2020).

\*Corresponding author

 [tarumi.kotaro.jp@gmail.com](mailto:tarumi.kotaro.jp@gmail.com) (K. Tarumi)

ORCID(s): 0009-0002-9030-5408 (K. Tarumi); 0000-0003-2282-3748 (K. Yoshizawa)

 <https://twitter.com/<@mil\protect\T1\textunderscoreglobalseis>> (K. Tarumi)

50 Many earlier tomography models based on surface wave data have provided valuable insights into the seismic  
51 structure of the continental upper mantle (e.g., Debayle and Kennett, 2000; Yoshizawa and Kennett, 2004; Yuan  
52 et al., 2011), revealing the thick lithosphere in continental cratons and the thinner lithosphere in younger, tectonically  
53 active regions (Fischer et al., 2020). However, surface wave approaches have intrinsic limitations in constraining upper  
54 mantle interfaces, as the long wavelengths of surface waves are insensitive to sharp velocity gradients. In contrast,  
55 teleseismic receiver functions (RFs) have been widely used to image the upper mantle discontinuities, owing to their  
56 good sensitivities to impedance contrasts and their capability to identify conversions of P-to-S (Ps) or S-to-P (Sp)  
57 phases across interfaces (e.g., Rychert et al., 2005, 2007; Abt et al., 2010; Ford et al., 2010; Liu et al., 2020; Rein  
58 et al., 2020).

59 Recent RF studies analyzing Sp conversions have reported enigmatic interfaces beneath continental cratons,  
60 associated with sharp S-wave speed reductions above the Lithosphere-Asthenosphere Boundary (LAB), known as  
61 the Mid-Lithospheric Discontinuity (MLD) (Fischer et al., 2010, 2020). Like the LAB, the MLD is key to unraveling  
62 ancient tectonic history preserved within the cratonic lithosphere. Moreover, other seismological studies have suggested  
63 the existence of an enigmatic X-discontinuity (or considered as the Lehmann discontinuity) beneath the LAB (Rein  
64 et al., 2020; Srinu et al., 2021; Pugh et al., 2021). However, unlike surface waves, RFs cannot directly constrain 3-D  
65 seismic velocity structures, leaving the spatial distribution and elastic properties of upper mantle discontinuities a  
66 subject of ongoing debate.

### 67 **1.1. Recent receiver function inversions**

68 Over the past few decades, numerous studies have combined surface wave dispersion (SWD) data with teleseismic  
69 RFs to overcome the inherent limitations of surface-wave and body-wave analyses (Julià et al., 2000; Vinnik et al., 2005;  
70 Bodin et al., 2012; Tkalčić et al., 2011; Bodin et al., 2014; Calò et al., 2016; Kim et al., 2016; Taira and Yoshizawa,  
71 2020; Ai et al., 2023). Recent joint inversion studies have utilized hierarchical trans-dimensional Bayesian inference to  
72 estimate seismic wave speed structures, including the depths of upper mantle discontinuities (e.g., Bodin et al., 2012,  
73 2014; Kim et al., 2016; Taira and Yoshizawa, 2020; Ai et al., 2023). However, this widely used joint inversion approach  
74 encounters challenges in imaging deep upper mantle discontinuities (e.g., LAB, X-D) due to the limited sensitivity of  
75 fundamental-mode SWD data and the reliance on stacked RFs.

76 Although SWDs enable us to constrain the absolute seismic shear velocity, the exclusive use of the fundamental  
77 modes limits the imaging of deeper structures below 200 km. The sensitivity of the fundamental mode SWDs  
78 diminishes significantly at greater depths, especially for Love wave (Figure S1). In contrast, surface wave overtones  
79 become sensitive to deeper structures, enabling better resolution throughout the entire upper mantle (e.g., Yoshizawa  
80 and Kennett, 2004; Yoshizawa and Ekström, 2010; Xu and Beghein, 2019). However, since multimode phase speed

81 measurements are not straightforward, several earlier studies employed only fundamental-mode SWDs (e.g., Calò  
82 et al., 2016). To enhance vertical resolution, Taira and Yoshizawa (2020) incorporated multimode SWDs into joint  
83 inversions with the P-wave RFs (P-RFs).

84 While RF inversions typically rely on stacked RFs derived from numerous individual RFs from many events, this  
85 approach presents two major difficulties due to intrinsic issues in the stacking process: the dependence of RF data on  
86 the range of epicentral distances and the back-azimuth of seismic events. The first issue is related to the moveout effect  
87 arisen from dependence on the distance range. This effect results in relative travel time differences between a parent  
88 phase (P-wave for P-RFs; S-wave for S-RFs) and the daughter phases (S for P-RFs; P for S-RFs), which vary with  
89 epicentral distance (or the slowness) (e.g., Kind and Yuan, 2011). To address this issue, conventional RF inversion  
90 studies have often limited the range of epicentral distances (e.g., Bodin et al., 2014; Calò et al., 2016; Taira and  
91 Yoshizawa, 2020). The second issue is the azimuthal dependence of RFs on the incoming direction of teleseismic  
92 parent waves, which results from lateral variations in seismic structure and the presence of layered anisotropic media  
93 with a horizontal symmetry axis (i.e., the azimuthal anisotropy) (Levin and Park, 1997; Frederiksen and Bostock, 2000;  
94 Frederiksen et al., 2003; Tonegawa et al., 2005; Nagaya et al., 2008; Kumar et al., 2011; Park and Levin, 2016).

95 These issues are generally neglected in many RF studies that employ either time-to-depth migration or inversions  
96 for velocity profiles (e.g., Rychert et al., 2005; Abt et al., 2010; Ford et al., 2010; Bodin et al., 2014; Taira and  
97 Yoshizawa, 2020; Birkey et al., 2021). However, such azimuth-dependent RFs have proven useful for imaging laterally  
98 heterogeneous structures through common conversion point (CCP) stacking, both in subduction zones (e.g., Tonegawa  
99 et al., 2005; Gilbert et al., 2006; Shi et al., 2015; Cheng et al., 2017; Kim et al., 2021) and continental regions (e.g.  
100 Kind et al., 2012; Sippl, 2016; Kennett and Sippl, 2018; Kind et al., 2020)). Although CCP stacking can yield clear  
101 structural images, it requires a dense station distribution, which is not always available in target research areas. Azimuth-  
102 dependent RFs have also been used to map crustal and mantle azimuthal anisotropy (Shiomi and Park, 2008; Nagaya  
103 et al., 2008; Bianchi et al., 2010; Nagaya et al., 2011; Ford et al., 2016; Chen et al., 2021). Bodin et al. (2016) pioneered  
104 the use of azimuth-dependent P-RFs in the trans-dimensional inversion to estimate azimuthal anisotropy beneath a  
105 station. However, no studies have yet attempted to image lateral variations in seismic interfaces through inversion.

106 Calò et al. (2016) employed the azimuth-dependent dataset of P-RFs to examine differences in inversion results.  
107 Although they observed variations in the inverted shear wave profiles and discontinuity depths, they did not account for  
108 these azimuthal effects. If rapid changes in discontinuity depth exist beneath a station, performing multiple inversions  
109 with RF datasets from different azimuth groups could capture such localized variations, potentially offering deeper  
110 insights into seismic interfaces, even from a single station.

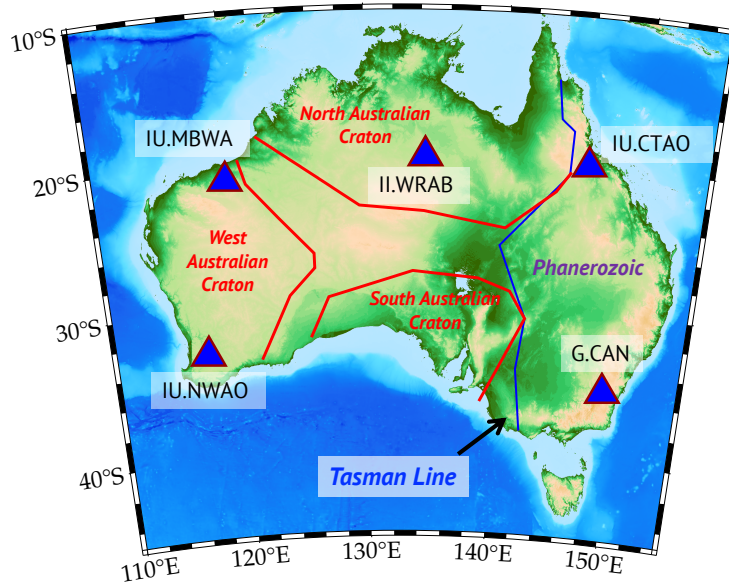


**Figure 1:** Map of the study region showing the locations of employed permanent stations (triangles). Red lines represent the cratonic margins of the North Australian Craton (NAC), South Australian Craton (SAC), and West Australian Craton (WAC). The blue line delineates the Tasman Line, the surface geological boundary separating cratonic regions in central and western Australia from the Phanerozoic basement in eastern Australia.

## 1.2. Australian tectonics and the scope of this paper

The Australian continent is the fastest-moving continental plate, drifting at about 6–7 cm/year (Argus et al., 2011), which was formed through ancient collisions of three major cratons - the West Australian Craton (WAC), the North Australian Craton (NAC), and the South Australian Cratons (SAC) - during the Proterozoic era (1.3–1.0 Ga) (e.g., Myers et al., 1996; Yoshida and Yoshizawa, 2020). The present-day continent comprises cratonic regions in central and western Australia and the eastern province formed by the Phanerozoic orogeny (Figure 1). Previous three-dimensional shear wave speed models from surface-wave tomography (e.g., Fishwick et al., 2008; Kennett et al., 2013; Yoshizawa, 2014; Magrini et al., 2023) have revealed the large-scale lithosphere-asthenosphere system beneath the Australian continent. The Australian LAB is relatively flat across the cratonic zones but rapidly deepens westward in Phanerozoic eastern Australia (e.g., Kennett et al., 2013; Yoshizawa, 2014; Davies et al., 2015; Magrini et al., 2023). Based on multimode surface-wave tomography, Fishwick et al. (2008) proposed a stepwise lithospheric change from east (100 km) to west (100–150 km), potentially inducing strong azimuthal dependencies in P-RFs.

In this study, we aim to estimate localized variations in the depths of upper mantle discontinuities using azimuth-dependent P-RFs. We incorporated azimuth-dependent P-RFs into the joint Bayesian inversion with multimode SWDs (Taira and Yoshizawa, 2020) and applied this approach to five long-standing permanent stations in the Australian continent (Figure 1). We then compiled multiple inversion results to map Ps conversion depths around each station,

127 revealing new insights into Australian upper mantle discontinuities. Our key findings on the MLDs and X-Ds provide  
128 valuable clues to understanding the spatial distribution and physical properties of these interfaces.

## 129 **2. Data sets**

130 Here, we summarize our data sets of multimode phase speeds of Rayleigh and Love waves (surface wave dispersions:  
131 SWDs) and P-to-S receiver functions (P-RFs), which are used in the joint inversion analyses described in the following  
132 section.

### 133 **2.1. Multi-mode surface-wave dispersion**

134 Our SWD dataset is based on the phase speed maps constructed by Yoshizawa (2014), as used by Taira and  
135 Yoshizawa (2020). This dataset from Yoshizawa (2014) comprises regional-scale multi-mode phase speed maps that  
136 cover Australia and surrounding regions.

137 Yoshizawa (2014) initially performed non-linear waveform fitting to measure path-averaged multimode phase  
138 speeds ray path. This method, originating with Yoshizawa and Kennett (2002b), was further refined with empirical  
139 criteria to automatically extract the multi-mode dispersion data (Yoshizawa and Ekström, 2010). Although overtone  
140 phase speed measurements are challenging due to the overlap of multiple modes, the fully nonlinear waveform fitting  
141 approach effectively extracts phase speed information for multimode surface waves (Yoshizawa and Kennett, 2002b;  
142 Yoshizawa and Ekström, 2010; Xu and Beghein, 2019). This method has also been applied to seismic records from  
143 Mars (Xu et al., 2021) and ambient noise tomography (Takagi and Nishida, 2022). In the second step, Yoshizawa  
144 (2014) performed 2-D mapping of the measured multimode phase speeds, incorporating the finite-frequency effects  
145 on seismic surface waves using the influence zone concept from Yoshizawa and Kennett (2002a). Including finite-  
146 frequency effects accounts for lateral heterogeneities around the great-circle path between a source and a receiver,  
147 resulting in a high-quality multimode SWD database.

148 From these multimode phase velocity maps, we extract localized dispersion curves at each station. Extracted phase  
149 speed dispersion diagrams are shown in Figure S2. Surface wave overtones are sensitive to structures below 200 km  
150 depth (Figure S1), while the fundamental mode sensitivity is limited to shallower depths (< 200km), particularly with  
151 the rapid decay of the sensitivity kernel for the fundamental Love wave. This limited sensitivity results in reduced  
152 resolution of SH wave speed or radial anisotropy structures. Taira and Yoshizawa (2020) demonstrated that higher-  
153 mode dispersion curves enhanced the vertical resolution of radially anisotropic structures. Following previous research,  
154 we use phase speed dispersion data from the fundamental up to the 4th higher mode. The period ranges for each mode  
155 of Rayleigh and Love waves used in this study are summarized in Table 1.

| Mode        | Rayleigh   | Love       |
|-------------|------------|------------|
| Fundamental | 30 – 200 s | 30 – 200 s |
| 1st         | 35 – 170 s | 33 – 170 s |
| 2nd         | 55 – 150 s | 60 – 125 s |
| 3rd         | 45 – 90 s  | 50 – 95 s  |
| 4th         | 35 – 65 s  | 45 – 70 s  |

**Table 1**

Period ranges of surface wave dispersion data. Ordinal numbers indicate overtones.

## 2.2. Azimuth-dependent P-wave receiver functions for permanent stations

We used three-component broadband seismograms, rotating the two horizontal components into radial and transverse components. P-RFs were estimated by deconvolving the vertical component from the radial component (Langston, 1979). While our waveform processing generally follows Taira and Yoshizawa (2020), we made minor updates to the deconvolution method and treatment of azimuthal dependencies in P-RFs. To accurately handle azimuth-dependent P-RFs, we made collections of horizontal misorientations of each station using our station orientation catalog available through the Zenodo repository (Tarumi and Yoshizawa, 2024).

For waveform processing, we selected events with moment magnitudes between 5.5 and 7.5, normalized P-wave radiation above  $|0.5|$  (from the Global CMT catalog (Dziewonski et al., 1981; Ekström et al., 2012)), epicentral distances between 30 and 90 degrees, and event depths less than 300 km. Figure 4 (e) shows the distribution of all selected events, and Figure S3 displays employed event distributions for each station. Seismograms were bandpass-filtered in two frequency ranges (0.03–0.2 Hz and 0.03–0.5 Hz). We discarded low-quality waveforms with S/N ratios below 5 on the vertical component and below 3 on the radial component. We then deconvolved the vertical component from the radial component based on the multi-taper receiver function technique (Shibutani et al., 2008), applying a water-level of 0.1% for the maximum amplitude in the frequency domain to stabilize spectral division in the frequency domain, instead of a Gaussian high-cut filter as introduced in the original method of Shibutani et al. (2008).

Conventional RF inversion studies, particularly in continental regions, generally stack large amounts of P-RF data while restricting events in a limited range of epicentral distance and/or back-azimuth (e.g., Julià et al., 2000; Bodin et al., 2012; Vinnik et al., 2014; Kim et al., 2016; Calò et al., 2016; Taira and Yoshizawa, 2020; Akuhara et al., 2021). The stacked RF is often treated as an averaged P-RF, representing a 1-D stratified structure around the station and neglecting azimuthal variations due to the incoming direction of P-waves. However, P-RFs are sensitive to the back-azimuth of events, as they reflect lateral structural changes or anisotropic layering around the station (e.g., Tonegawa et al., 2005; Kumar et al., 2011). Teleseismic P-waves are converted to S-waves when transversing structural boundaries, so rapid lateral variations in seismic structure beneath a station induce significant back-azimuthal dependencies in P-RFs on the incoming P-wave direction (e.g., Figure 3 (b)). These azimuthal dependencies in RFs,

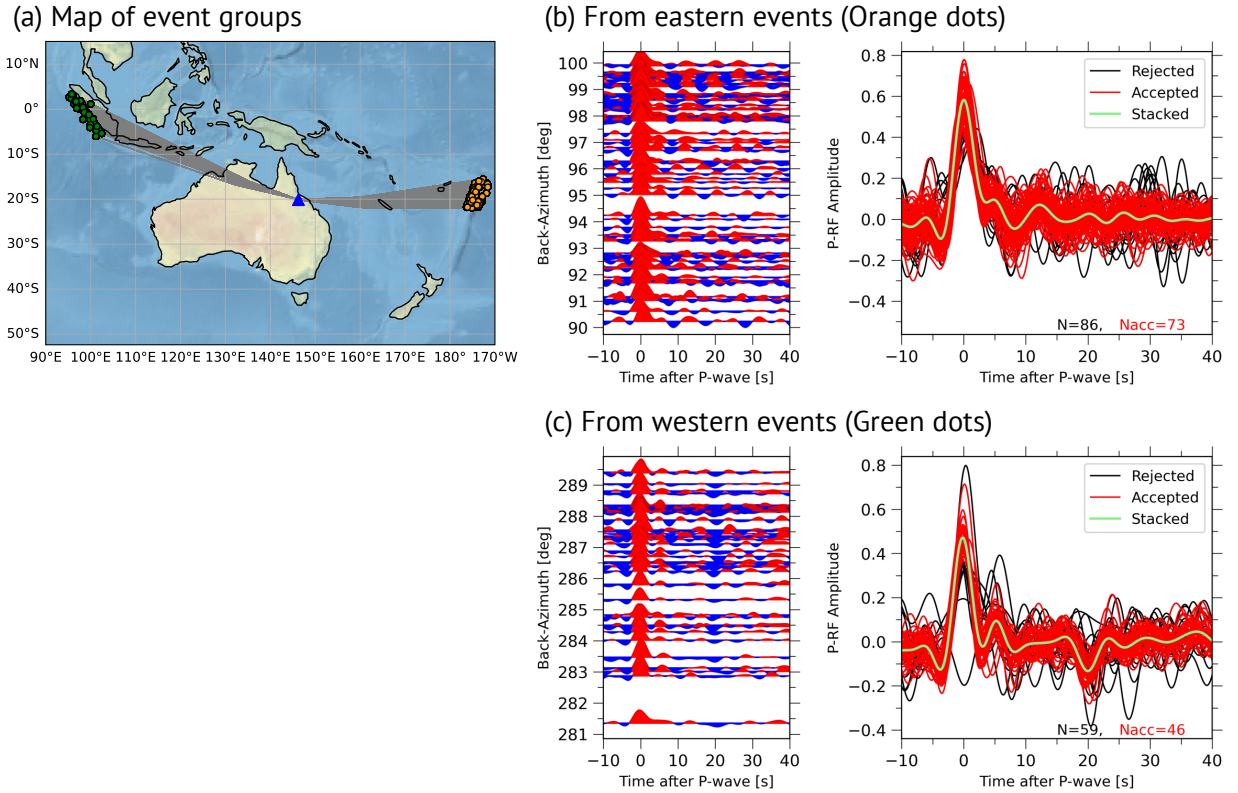


**Figure 2:** Example of the binned-stacking process for P-RFs at CTAO. (a) Map of seismic events for two groups, with orange and green dots representing eastern and western events, respectively. Gray lines indicate ray paths from each event location to the station. (b) P-RF stacking process for the eastern event group (orange dots in (a)) with a back-azimuth range between  $90^\circ$  and  $100^\circ$ . The left panel shows individual P-RF traces that meet all selection criteria outlined in the main text, with positive and negative phases filled in red and blue. The right panel shows the stacking process, where green, red, and black lines represent stacked, accepted, and rejected traces based on cross-correlation selection.  $N$  and  $N_{acc}$  denote the total number of traces and the number of accepted traces, respectively. (c) Same as (b) but for the western event group (green dots in (a)).

181 which have been neglected in earlier studies (e.g., Taira and Yoshizawa, 2020), can be potentially useful for mapping  
 182 localized lateral changes in P-to-S conversion points.

183 To utilize the azimuthal dependencies in P-RFs that reflect the lateral changes in interface depths, we adopt a  
 184 binned-stack approach with 10-degree ranges and intervals for both epicentral distance and back-azimuth to estimate the  
 185 azimuth-dependent P-RFs. To maintain a high-quality dataset in this stacking process, we employ the cross-correlation-  
 186 based selection method (Tkalčić et al., 2011), as in Taira and Yoshizawa (2020). This method selects P-RF traces for  
 187 stacking based on normalized cross-correlation coefficients (NCC) between all P-RF pairs. In this study, we grouped  
 188 P-RF traces with  $NCC > 0.8$  for the 0.03–0.2 Hz range and  $NCC > 0.7$  for the 0.03–0.5 Hz range, discarding groups  
 189 with fewer than 10 traces.

190 Figure 2 shows examples of azimuth-dependent P-RF dataset for CTAO, located in northwestern Australia. Figure  
 191 2 (a) presents a map of events used to compute the RFs visualized in Figures 2 (b) and (c). While both P-RFs reflect

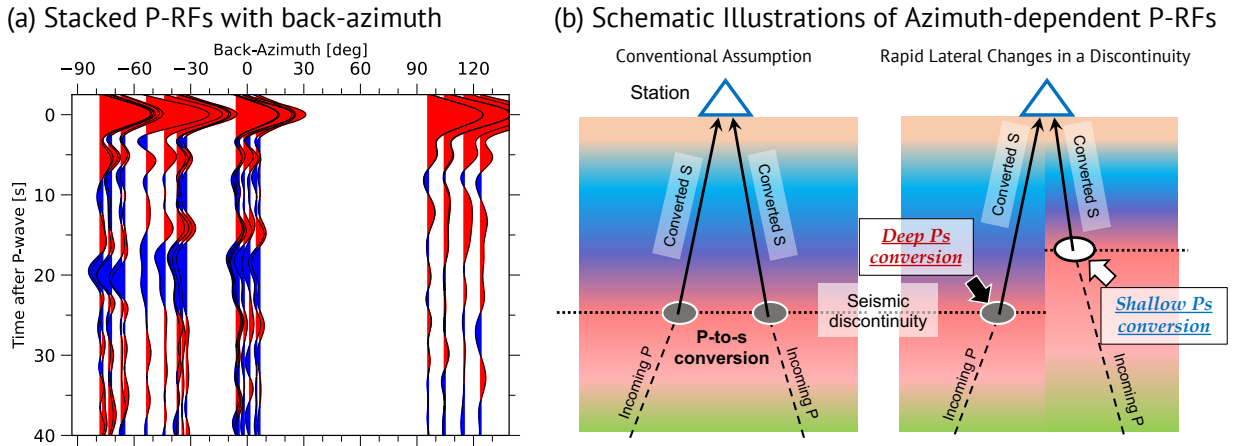


**Figure 3:** Azimuth-dependent P-RF dataset for CTAO and schematic illustrations of azimuthal dependence in P-RFs. (a) Compilation of stacked P-RF traces at CTAO with respect to back-azimuth, measured clockwise from the north. The color scheme for filled phases is the same as the right panels in Figures 2 (b and c). (b) Schematic illustrations of potential origins of azimuthal dependence in P-RFs. The left panel shows the P-to-S conversion assuming a 1-D stratified model, where conversion locations are independent of the incoming P-wave directions. In contrast, the right panel illustrates a scenario with rapid lateral structural changes around the seismic station, where conversion points vary with the event's azimuth.

192 the seismic structure beneath CTAO, the expected conversion points differ laterally by 100–150 km at 200 km depths.  
 193 In Figures 2 (b) and (c), distinct differences in the shapes of back-azimuth-ordered and stacked RFs are visible (e.g., at  
 194 5, 8, and 20 s). Around 5 s, the stacked P-RF from western events (green line in Figure 2 (c)) clearly exhibits a positive  
 195 signal, which is unclear in the stacked P-RF from eastern events (green line in Figure 2 (b)). Around 8 s in the eastern  
 196 P-RFs (Figure 2 (b)) and 20 s in the western P-RFs (Figure 2 (c)), strong negative phases are evident. Besides, these  
 197 differences in azimuth-dependent P-RFs seem to be coherent within each back-azimuth range (left panels in Figures 2  
 198 (b, c)), implying structural variations beneath the station along the ray-paths.

199 Figure 3 (a) displays a compilation of stacked P-RFs at CTAO as a function of back-azimuth, along with a schematic  
 200 illustration of the plausible origin of these azimuthal dependencies. Figure S4 shows the frequency dependence of  
 201 azimuth-dependent P-RFs at CTAO, covering four frequency ranges (i.e., 0.03–0.125 Hz; 0.03–0.2 Hz; 0.03–0.5 Hz;  
 202 0.04–1.0 Hz). In Figure 3 (a), as described, P-to-S conversions appear as isolated phases at around 5 s in the western  
 203 and northern directions, whereas in the east, these conversions become less distinct due to overlap with the direct  
 204 P-wave. In higher frequency ranges (Figure S4 (c, d)), the positive phases at 5 s are more prominent than in lower  
 205 frequency P-RFs (Figure 3 (a)). Additionally, at higher frequencies, remarkable differences also emerge before the  
 206 Moho conversions, potentially indicating lateral variations in crustal structure, although this is beyond our current  
 207 scope. In the later phases (after 5 s), significant negative phases around 20 s appear in the west and north directions,  
 208 but these negative phases are absent in the eastern P-RFs. These trends remain consistent in higher frequency P-RFs

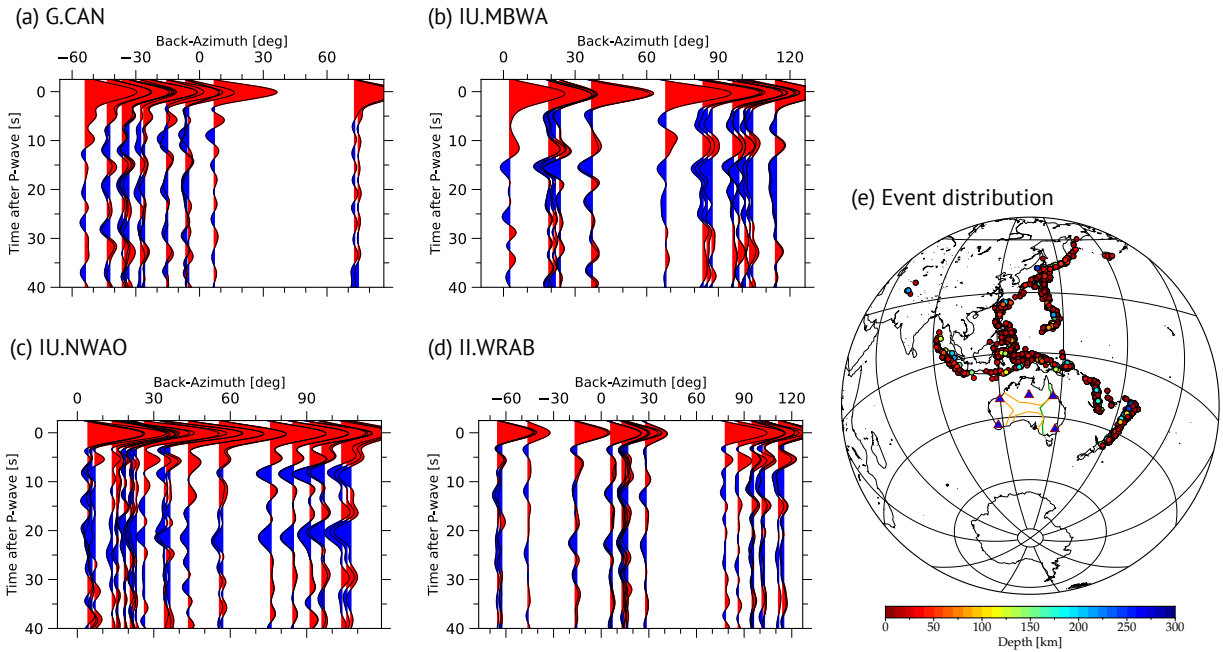


**Figure 4:** (a–d) Azimuth-dependent P-RF datasets (0.03–0.2 Hz) of the four stations used in this study: (a) G.CAN, (b) IU.MBWA, (c) IU.NWAO, and (d) II.WRAB. Figure notations are the same as Figure 3 (a). (e) Map of all events used in this study, with blue triangles indicating station locations and colored circles representing individual seismic events. Yellow and green lines delineate the major cratonic boundaries and the Tasman Line.

209 (Figure S4) and are robust, though they become slightly less clear due to contamination from multiple reflections from  
 210 the Moho, shallower interfaces, and other scattered phases.

211 The significant negative phases at 20 s likely originate from a rapid velocity reduction in the upper mantle. Around  
 212 CTAO, previous tomographic models have suggested that the upper mantle structure undergoes rapid lateral changes,  
 213 possibly reflecting the transition between the eastern Phanerozoic and western cratonic regions (e.g., Fishwick et al.,  
 214 2008; Yoshizawa, 2014; de Laat et al., 2023). Figure 3 (b) provides a schematic illustration of Ps conversion points  
 215 with and without such structural changes. Conventional RF studies in continental regions have implicitly assumed a  
 216 1-D stratified layered model beneath the station (left panel in Figure 3 (b)). However, in the scenario depicted in the  
 217 right panel of Figure 3 (b), the conversion points from P to S vary with the incoming direction of teleseismic P-waves,  
 218 which serve as the parent phase for the converted S-waves. The azimuth-dependent P-RFs observed at CTAO likely  
 219 result from lateral localized variations in the upper mantle interface.

220 Figure 4 shows azimuth-dependent P-RF datasets (0.03–0.2 Hz) at four stations, excluding CTAO: (a) G.CAN (b)  
 221 IU.MBWA, (c) IU.NWAO, and (d) II.WRAB. Figure S5 presents the shorter-period datasets (0.03–0.5 Hz) for these  
 222 stations. Except for MBWA (Figure 4 (b)), clear positive conversion phases are observed at 5–6 s in Figures 4 (a), (c),  
 223 and (d), suggesting the thick crust or the deep Moho (Kennett et al., 2023). On the contrary, the lack of positive phases

at 5 s in MBWA may indicate the thinner crust, around 30 km in thickness (e.g., Taira and Yoshizawa, 2020; Kennett et al., 2023), which is also shown in Figure S5 (b). As shown in MBWA (Figure 4 (b)), long-period P-RFs may not adequately constrain the Moho depth and crustal structure in regions with thinner crust. Thus, we used higher-frequency data (0.03–0.5 Hz) from 10 s after the main P-phase in the inversion process described in the next section. For four stations (Figure 4 (a-d)), the later phases after 5–6 s indicate the azimuthal dependence, though this tendency is weaker compared to CTAO (Figure 3 (a)), implying that lateral variations in seismic structure beneath these stations may be milder.

### 3. Trans-dimensional Bayesian inversion

We apply hierarchical trans-dimensional Bayesian inference (Bodin et al., 2012) to invert azimuth-dependent P-RFs and multimode SWDs (phase speeds of Rayleigh and Love waves). This probabilistic approach allows for flexible sampling of model parameters and requests fewer a priori constraints than traditional linearized inversion methods. The trans-dimensional algorithm treats both the number of parameters (e.g., the number of layers) and data uncertainties as unknowns, allowing for exploration across the entire model parameter space. We consider the Bayesian theorem extended into a hierarchical trans-dimensional formulation as follows,

$$p(\mathbf{m}(k), k, \sigma | \mathbf{d}) \propto p(\mathbf{d} | \mathbf{m}(k), k, \sigma) p(\mathbf{m}(k)) p(k) p(\sigma), \quad (1)$$

where  $p(A|B)$  is the conditional probability density function (p.d.f.) of the occurrence of A given B.  $p(m(k), k, \sigma | d)$ ,  $p(d | m(k), k, \sigma)$ ,  $p(m(k))$ ,  $p(k)$ , and  $p(\sigma)$  represent the posterior, likelihood, model prior, hyperpriors for the number of model parameters and the data noise, respectively. To estimate the posterior probability, we employ the reversible-jump Markov chain Monte Carlo (RJMCMC) method (Green, 1995), which efficiently samples model parameters to fit the observed data.

#### 3.1. Model parameterization

In this study, we assume a one-dimensional stratified structure beneath each station. The stratified model parameters follow Taira and Yoshizawa (2020), comprising interface depths  $z$  and perturbations in SV and SH wave velocities from the reference model,  $\delta V_{SV}$  and  $\delta V_{SH}$ . Using the hierarchical trans-dimensional scheme, we also include data noises  $\sigma$  for two frequency ranges of P-RFs and each mode of multimode SWDs  $\sigma$ , as well as the number of layers  $k$  as parameters to be recovered. Thus, the model parameter vector  $\mathbf{m}$  is defined as  $[\sigma, k, z, \delta \mathbf{V}_{SV}, \delta \mathbf{V}_{SH}]$ .

The spherical radially anisotropic S-wave model is perturbed to the 400 km depth, combined with the PREM (Dziewonski and Anderson, 1981) below 400 km. Other elastic parameters are scaled based on the shear-velocity structure and replaced by the 1-D reference model. For P-waves, we maintain the fixed ratio between  $V_P$  and  $V_S$  to the

AK135 model (Kennett et al., 1995) and calculate  $V_P$  from  $V_S$ . The density structure  $\rho$  is scaled with compressional wave speeds through the empirical relationship  $\rho = 2.35 + 0.036(V_P - 3)^2$  (e.g., Tkalčić et al., 2006; Bodin et al., 2012, 2014; Taira and Yoshizawa, 2020). The radial anisotropy parameter  $\eta$  and anelastic attenuation values of  $Q_\kappa$  and  $Q_\mu$  are fixed to a modified PREM where the 220 km discontinuity is smoothed.

### 3.2. The prior

Prior probabilities for model parameters are defined using uniform or normal distributions. For the number of parameters  $k$  and data uncertainties  $\sigma$ , we assume uniform distributions over the ranges [5, 61] and [0.01, 0.2], respectively. The prior for the depth is uniformly distributed from 0 to 400 km.

For S-wave perturbations, we use a zero-mean Gaussian prior with a standard deviation of  $\sigma = 0.3$  km/s, following Akuhara et al. (2021) and Ai et al. (2023). Local reference models for each station are derived from the three-dimensional radially anisotropic S-wave speed model by Yoshizawa (2014), which has been optimized for multimode SWDs through linearized inversions, providing good resolution in the deep upper mantle. The crustal model, however, is approximated using the 3SMAC model (Nataf and Ricard, 1996) since phase velocities from seismic surface waves at periods longer than 30 s have limited sensitivity to shallow structures. To represent the Australian crustal structure accurately, we replace the crustal SV velocity model of Yoshizawa (2014) with the AuSREM crustal S-wave speed model and local Moho depth (Kennett et al., 2011; Salmon et al., 2013; Kennett et al., 2023). Radial anisotropy is fixed to the Yoshizawa (2014) model. As a result, our local reference model reflects both the crustal and upper mantle structure of Australia. Figure S7 displays the reference structural model used for each station.

### 3.3. Likelihood function

The likelihood functions measure the consistency between synthetic and observed data. Since we incorporate both surface-wave dispersion curves and P-RFs, our likelihood term is defined by the joint probability:

$$p(\mathbf{d}|\mathbf{m}(k), \sigma) = p(\mathbf{d}_{\text{SWD}}|\mathbf{m}(k), \sigma_{\text{SWD}}) p(\mathbf{d}_{\text{PRF}}|\mathbf{m}(k), \sigma_{\text{PRF}}), \quad (2)$$

where the first and second terms in the right-hand of (eq. 2) correspond to the likelihood probability density functions for SWD and P-RF, respectively. These are formulated based on the Gaussian distributions following Taira and Yoshizawa (2020):

$$p(\mathbf{d}_{\text{SWD}}|\mathbf{m}(k), \sigma_{\text{SWD}}) = \prod_{i=0}^4 \frac{1}{\sigma_i^R \sqrt{(2\pi)^{N_{R_i}}}} \exp\left(-\frac{\|\mathbf{d}_i^R - \mathbf{g}_i^R(\mathbf{m}(k))\|^2}{2\sigma_i^{R,2}}\right) \quad (3)$$

$$\times \prod_{i=0}^4 \frac{1}{\sigma_i^L \sqrt{(2\pi)^{N_{L_i}}}} \exp\left(-\frac{\|\mathbf{d}_i^L - \mathbf{g}_i^L(\mathbf{m}(k))\|^2}{2\sigma_i^{L,2}}\right), \quad (4)$$

276 and

$$p(\mathbf{d}_{\text{PRF}} \parallel \mathbf{m}(k), \sigma_{\text{PRF}}) = \prod_{i=1}^2 \frac{1}{\sigma_i^{\text{PRF}} \sqrt{(2\pi)^{N_{\text{PRF}_i}}}} \exp\left(-\frac{\|\mathbf{d}_i^{\text{PRF}} - \mathbf{g}_i^{\text{PRF}}(\mathbf{m}(k))\|^2}{2\sigma_i^{\text{PRF},2}}\right), \quad (5)$$

277 where  $\mathbf{d}^R$ ,  $\mathbf{d}^L$ , and  $\mathbf{d}^{\text{PRF}}$  represent the observed data for Rayleigh and Love wave dispersion curves and P-RFs,  
 278 respectively, and  $\mathbf{g}^R$ ,  $\mathbf{g}^L$ , and  $\mathbf{g}^{\text{PRF}}$  denote the forward-modeled data for each dataset. For synthetic data calculations,  
 279 we use the normal mode theory (DISPER80; TAKEUCHI and SAITO, 1972; Saito, 1988) for SWD computations and  
 280 the Thomson-Haskell method (Thomson, 1950; Haskell, 1962) for P-RF modeling, which is widely used in Monte-  
 281 Carlo inversion studies (e.g., Bodin et al., 2012, 2016; Calò et al., 2016; Taira and Yoshizawa, 2020). Since these  
 282 approaches are based on a 1-D stratified flat Earth model, we apply an Earth-flattening correction to account for the  
 283 spherical Earth model.

284 To investigate the lateral variations of discontinuity depths, we performed inversions using local SWDs from the  
 285 surface-wave tomography model as well as P-RFs for each azimuth-distance bin. Note that the local multimode SWDs  
 286 were fixed for each station (Figure S2) because they reflect the local seismic structure around a seismic station as seen  
 287 by long-wavelength surface waves.

### 288 3.4. Reversible-jump sampling with Parallel Tempering

289 To estimate ensemble solutions, we use the reversible-jump Markov chain Monte Carlo (RJMCMC) scheme (Green,  
 290 1995). RJMCMC aims to infer the posterior density of model parameters by iteratively exploring model parameter  
 291 spaces of varying dimensions. In each iteration, a new model parameter vector is proposed by randomly selecting  
 292 one of several perturbation patterns: (1) create a new layer, (2) remove a layer, (3) perturb a data error, (4) adjust a  
 293 transition depth, (5) perturb the SV wave speed in a layer, or (6) perturb the SH wave speed in a layer. We then compute  
 294 the synthetic data and likelihood function based on the proposed model. The model acceptance is determined using  
 295 the Metropolis-Hastings (MH) algorithm (Metropolis et al., 1953; Hastings, 1970). To enhance convergence speed and  
 296 improve acceptance rates, we apply the Parallel Tempering (PT) method to the MH algorithm (Sambridge, 2014), as  
 297 implemented in Taira and Yoshizawa (2020) and Akuhara et al. (2021). PT enables broader exploration of the model  
 298 parameter space by running multiple Markov chains in parallel, each with a different temperature. Consequently, our  
 299 MH acceptance criterion, based on the likelihood probability, is expressed as:

$$\alpha_{MH} = \min\left\{1, \left[\frac{p(\mathbf{d} \parallel \mathbf{m}_j, k_j, \sigma_j)}{p(\mathbf{d} \parallel \mathbf{m}_i, k_i, \sigma_i)}\right]^{1/T_j} \times \left[\frac{p(\mathbf{d} \parallel \mathbf{m}_i, k_i, \sigma_i)}{p(\mathbf{d} \parallel \mathbf{m}_j, k_j, \sigma_j)}\right]^{1/T_i}\right\}, \quad (6)$$

300 where  $\alpha_{MH}$  is the acceptance probability in the PT framework, subscripts  $i$  and  $j$  denote the  $i$ -th and  $j$ -th MCMC  
 301 chains, and  $T_n$  is the temperature of the  $n$ -th chain. In PT, each chain runs in parallel at a different temperature. In this

302 study, we run 40 chains in parallel, 10 of which are set as unit temperature, while the remaining 30 chains have higher  
 303 temperatures following  $T_i = 200^{i/30}$ , resulting in a maximum temperature of 200 °C.

304 For RJMCMC sampling, we set the maximum iteration number of 150,000, discarding the initial 50,000 models  
 305 as the burn-in period. To avoid autocorrelated samples, we store the models at intervals of 100 iterations, resulting in  
 306 posterior distributions constructed from 10,000 models.

#### 307 4. Results of inversions for Australian stations

308 The trans-dimensional Bayesian inversion estimates the probability density functions of model parameters. From  
 309 these probabilistic models, we identify seismic discontinuities (i.e., Moho, LAB, MLDs, and X-Ds) based on S-wave  
 310 velocity changes through a combination of automated and visual inspections. Hereafter, we focus on the isotropic  
 311 S-wave speed derived by the voigt average,  $V_{S_{iso}} = \sqrt{\frac{2V_{SV}^2 + V_{SH}^2}{3}}$ , and the radial anisotropy,  $\xi = (\frac{V_{SH}}{V_{SV}})^2$ .

312 Using our posterior distributions, the Moho can be identified as the depth of the maximum positive  $V_{iso}$  jump,  
 313 mostly consistent with the AusMoho depth (Kennett et al., 2023) constructed by compiling multiple geophysical  
 314 datasets (e.g., reflection profiles and refraction explorations). S-wave speeds in the asthenosphere are generally slower  
 315 than the lithosphere, and the LAB is often characterized by the significant S-wave speed reduction in the upper mantle  
 316 (e.g., Kennett et al., 2013). Thus, we first imposed an isotropic S-wave speed of less than 4.7 km/s as an LAB criterion,  
 317 then determined the LAB as a  $V_{iso}$  or  $V_{SV}$  drop of over 0.04 km/s around the Lithosphere-Asthenosphere Transition  
 318 (LAT) identified by Yoshizawa (2014) from vertical gradients in shear wave speed profiles. However, at WRAB in  
 319 the southern North Australian Craton (NAC), the high isotropic S-wave speed extends to 200–300 km depth, and  
 320 no significant velocity reduction is observed within the LAT range. In such cases, we determined the depth of the  
 321 lithospheric base by identifying a positive jump in radial anisotropy,  $\xi$ , following Plomerová et al. (2002).

322 With the mantle lithosphere thickness defined, we identified MLDs within the mantle lithosphere and X-Ds  
 323 underlying the LAB or lithospheric base. MLDs are marked by a  $V_{iso}$  or  $V_{SV}$  change of at least 0.02 km/s above  
 324 the LAT upper bound or selected LAB depths and are detected primarily at stations in cratonic areas (MBWA, NWAO,  
 325 and WRAB). For X-Ds, we identified S-wave speed jumps of over 0.04 km/s beneath the selected LAB. Both MLDs  
 326 and X-Ds may occur at multiple depths. To examine the relationship between MLDs/X-Ds and the radial anisotropy  
 327 without bias, we did not adopt any criteria related to radial anisotropy when identifying MLDs and X-Ds.

328 This section discusses our results separately for the Phanerozoic and cratonic provinces of Australia. For the  
 329 Phanerozoic province, we present inversion results for CTAO and CAN (Figures 5 and 6). For cratonic regions, Figure  
 330 7 shows joint inversion results at two stations, MBWA and NWAO, in the WAC, and Figure 8 presents the results at  
 331 WRAB in the NAC. Employed event distributions are also displayed in Figures 5, 6, 7, and 8. Previously estimated  
 332 discontinuity depths from earlier studies (Yoshizawa, 2014; Birkey et al., 2021; Kennett et al., 2023) are superimposed

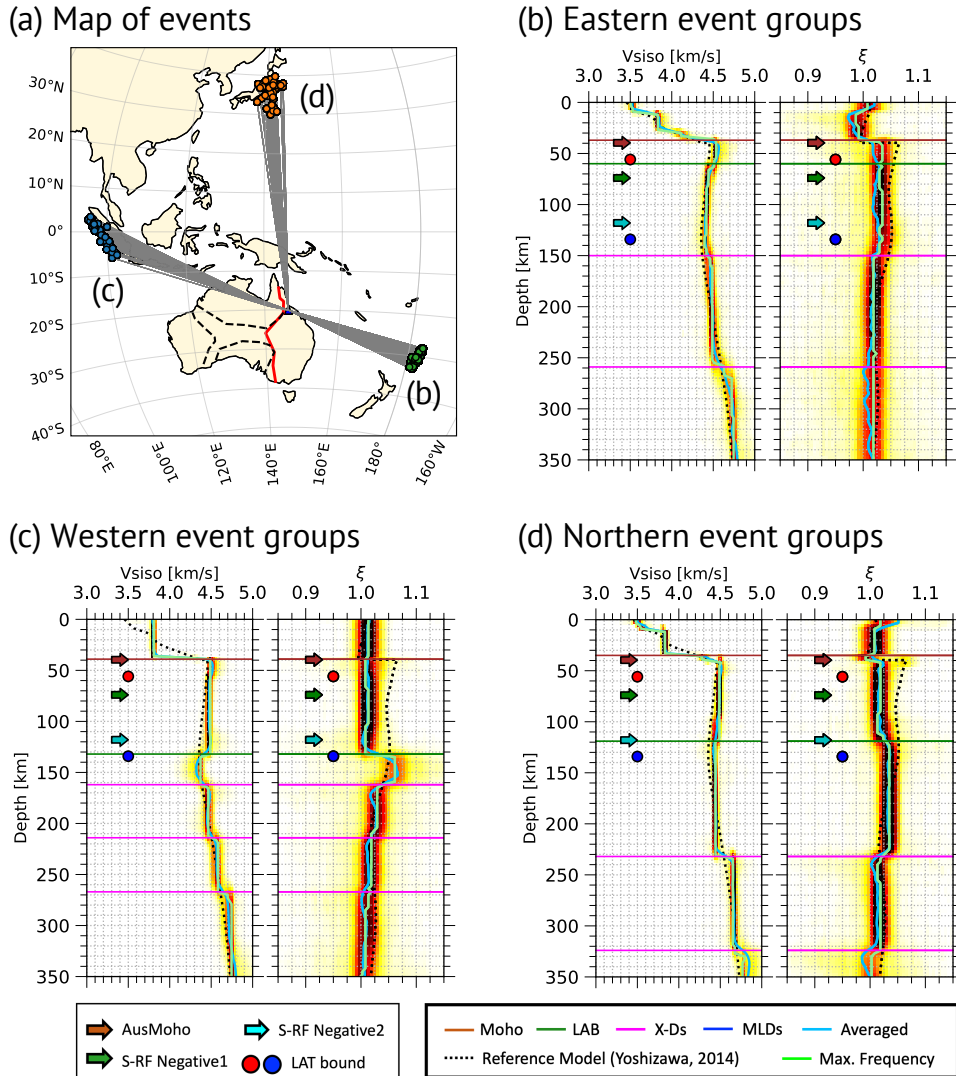


**Figure 5:** Examples of joint inversion results for CTAO. (a) Event distribution, with colored dots representing seismic events grouped by direction and a blue triangle indicating the target station. Black dotted and red lines are the major cratonic boundaries and the Tasman Line, respectively. (b) Posterior distributions of isotropic S-wave speed  $V_{iso}$  and radial anisotropy  $\xi$  retrieved from the eastern event group, with sky blue, purple, and light green lines indicating the mean and mode (maximum frequency) models, respectively. Black dotted lines show the reference model for the inversion. Colored horizontal lines are identified discontinuities (brown: Moho, blue: MLDs, green: LAB or Lithospheric base, magenta: X-Ds). Brown arrows indicate the AusMoho depth Kennett et al. (2023), while green and light blue arrows represent the depths of the first and second maximum negative peaks in S-RF profiles (Birkey et al., 2021). Red and blue dots exhibit the upper and lower depths of the Lithosphere-Asthenosphere Transition (LAT) derived from Yoshizawa (2014). All notations are shown at the bottom of the figure. (c, d) Same as (b), but for the western and northern event groups.

333 on the resultant 1-D profiles, including AusMoho depth, the first and second negative peaks in S-RF profiles from  
 334 Birkey et al. (2021), and LAT upper and lower bounds from Yoshizawa (2014), as indicated in each figure and caption.

## 4.1. Phanerozoic eastern Australia

### 4.1.1. CTAO station

Selected inversion results at the CTAO station for the eastern, western, and northern event groups are shown in Figure 5. Posterior distributions for hyperparameters (i.e., the number of layers and data noises) and data misfit distributions are summarized in Figures S7-S9. In the inversion results at CTAO, distinct azimuthal dependencies are observed in both isotropic S-wave and radial anisotropy profiles (Figure 5 (b–d)). The data misfits are sufficiently low, with each P-RF well reproduced (Figures S7, S8, and S9), indicating that the velocity structures are reliably resolved. Identified upper mantle discontinuities vary with the incident directions of teleseismic P-waves corresponding to each event group.

In all inversion results (Figure 5 (b–d)), we observe shear wave speed jumps at around 40 km, corresponding to the Moho, consistent with the AusMoho model (Kennett et al., 2023)) and Taira and Yoshizawa (2020). Some variations in crustal structures are present in the results for different event directions but are not discussed here, as our focus is on the upper mantle discontinuities. Note that our long-period SWD dataset has limited sensitivity to constrain the absolute shear velocity in the crust.

The LAB depths, marked by shear velocity reductions, vary by event group, suggesting lateral changes in lithospheric thickness. In the eastern results (Figure 5 (b)), an S-wave velocity drop appears at around 60 km within the LAT, which may be comparable to the S-RF's negative phase at 74 km (Birkey et al., 2021). Western and northern results show a deeper velocity drop at 120–130 km, above the lower bound of LAT (Figure 5 (c, d)), consistent with the second negative peak of S-RF at 118 km. Increasing radial anisotropy  $\xi$  across these interfaces (Figure 5 (b–d)) is consistent with the expected horizontal shear flow in the asthenosphere.

These findings suggest rapid lateral LAB depth variations around CTAO, from 60–70 km in the east to 120–130 km in the west and north, supporting a step-wise lithospheric model by Fishwick et al. (2008) and the azimuth-dependent variations seen in the P-RF profiles (Figure 3).

Below the LAB at CTAO, we identify multiple S-velocity jumps at around 170, 220, 270, and 330 km, consistent with Revenaugh and Jordan (1991), who proposed similar multiple discontinuities based on path-averaged ScS reverberations. They interpreted shallower interfaces around 170 and 220 km as the Lehmann discontinuity and the deeper interfaces as the X-Ds. Although we cannot decisively identify the Lehmann discontinuity, these multiple discontinuities, associated with positive S-velocity jumps, coincide with regions of weakened anisotropy, as noted in Taira and Yoshizawa (2020).

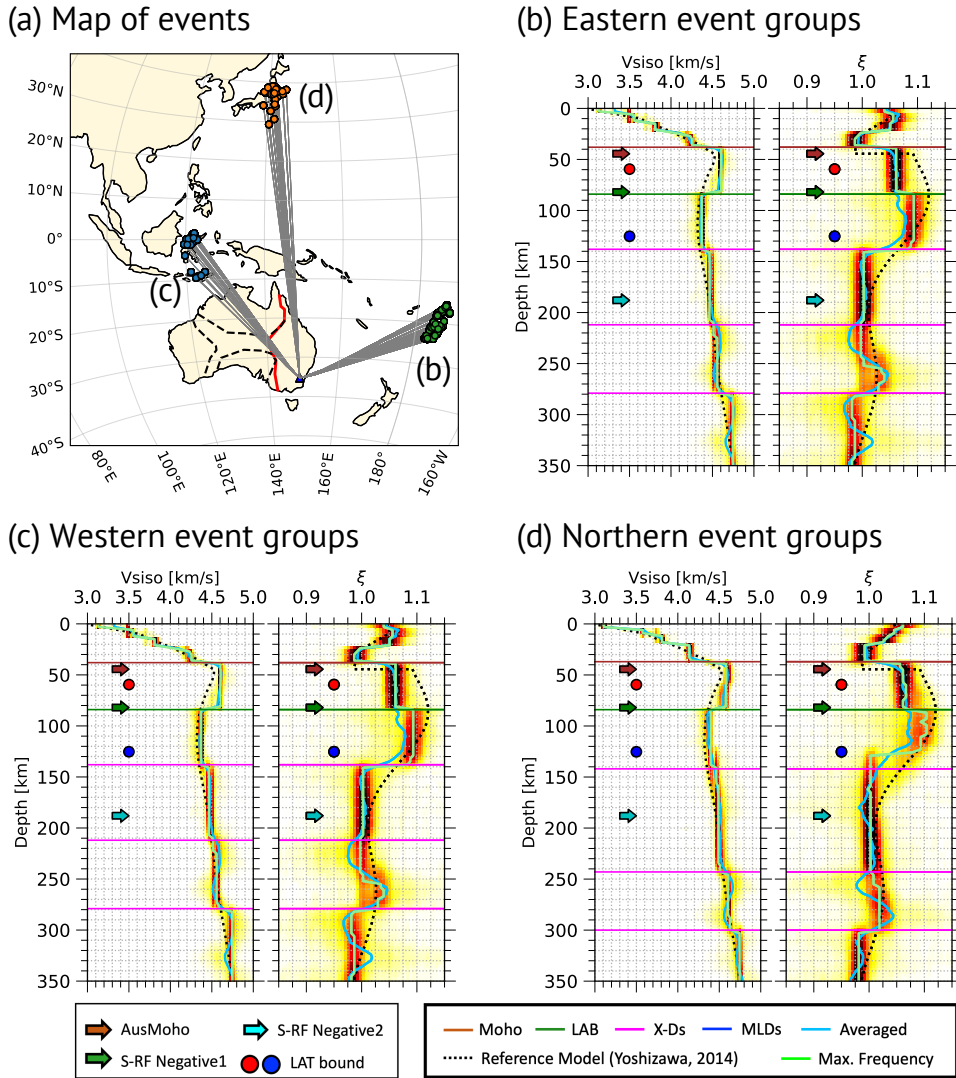


Figure 6: Same as 5, but for G.CAN.

364 **4.1.2. CAN station**

365 For the CAN station, inverted S-velocity profiles for different event groups are consistent (Figure 6), unlike the result  
 366 for CTAO in Figure 5. Clear S-wave velocity jumps at 40 km depth indicate the Moho, which is slightly shallower than  
 367 AusMoho. While the Australian Moho map (e.g., Kennett et al., 2023) suggests a locally thicker crust in southeastern  
 368 Australia, its northern area indicates a thinner crust, which may be reflected in our results. The LAB is identified by a  
 369 sharp velocity reduction at around 80 km depth within the LAT, similar to the S-RF negative peaks reported by Birkey  
 370 et al. (2021). Like CTAO, the LAB coincides with increased radial anisotropy, suggesting the effects of horizontal  
 371 mantle flow beneath it. Our data suggest an interface with a shear velocity drop at 65km depth, consistent with another  
 372 negative S-RF phase at 50–60 km in Birkey et al. (2021). Below the LAB, we detect multiple discontinuities with

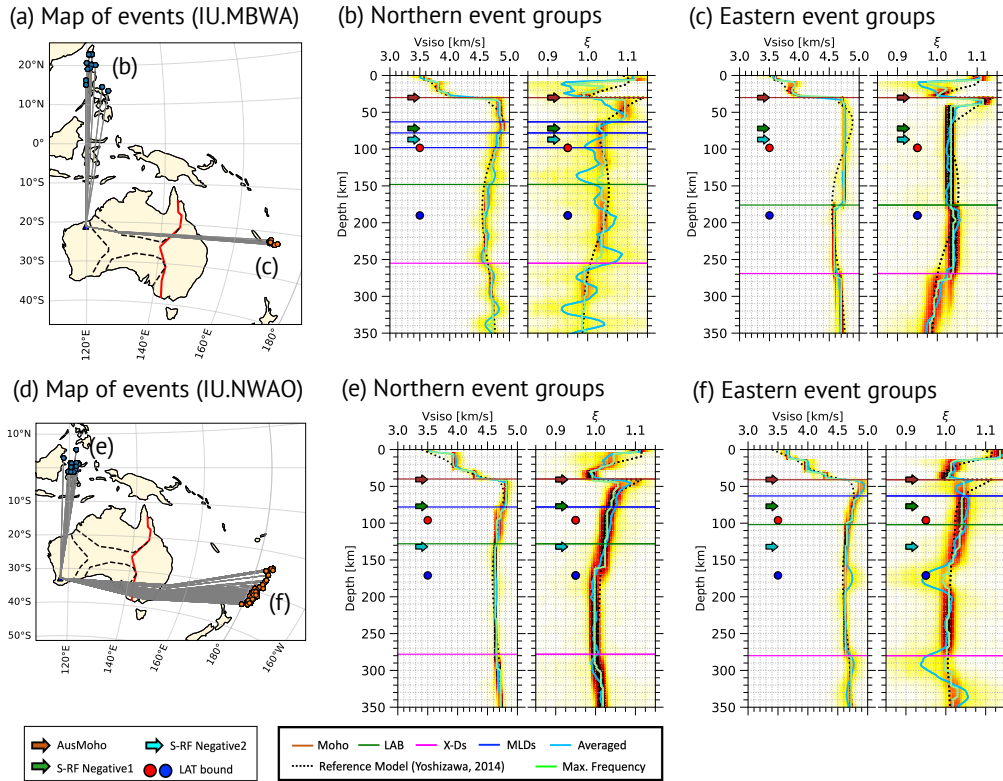


Figure 7: Same as Figure 5, but for IU.MBWA and IU.NWAO.

373 positive velocity gradients and similar anisotropy characteristics to CTAO, showing decreased  $\xi$ . The detected depths  
 374 are close to those at CTAO: 140–150 km, 220–260 km, and around 300 km.

## 375 4.2. Cratonic central and western Australia

### 376 4.2.1. MBWA and NWAO stations in western Australia

377 Figure 7 shows inversion results using multiple event groups for both the MBWA and NWAO stations located in  
 378 the Archean cratons. At MBWA located near the northeastern margin of the Pilbara craton, facing the suture zone  
 379 between WAC and NAC, azimuthal dependency is evident, likely due to the structural differences along the northern  
 380 and eastern paths (Figure 7 (b, c)). In contrast, NWAO located in the southwestern area of the Yilgarn craton, where  
 381 eastern and northern ray-paths propagate through the stable cratonic region, exhibits weaker azimuthal dependency  
 382 (Figure 7 (e, f)). Our results from the northern event groups are generally consistent with the S-RF studies (Birkey  
 383 et al., 2021).

384 At MBWA in Figure 7 (a-c), azimuth-independent Moho depths are observed around 30 km, consistent with  
 385 AusMoho (Kennett et al., 2023). The LAB, characterized by a shear velocity drop ( $> 0.04$  km/s), is estimated at  
 386 150 km in the north and 170–180 km in the east, with a weaker increase in radial anisotropy than in eastern Australia.

387 Multiple MLDs are identified at the lithospheric depths, consistent with previous studies (Taira and Yoshizawa, 2020;  
388 Sun et al., 2018), showing decreasing radial anisotropy across the MLDs as suggested by Yoshizawa and Kennett (2015)  
389 and Kennett et al. (2017). The second and third MLDs (Figure 7 (b)) exhibit negative velocity changes, supporting the  
390 earlier S-RF study by Birkey et al. (2021). A single X-D is observed at around 270 km, accompanying the weakening  
391 of radial anisotropy.

392 At NWAO in Figure 7 (d-f), azimuth-independent Moho depths are identified at 40 km. MLDs are found at a depth  
393 of 60 km in the eastern path and 80 km in the northern path, similar to the results from S-RF (Birkey et al., 2021).  
394 LAB signatures are detected at 130 km depth in the northern path, which is consistent with the second negative peak  
395 in S-RF by Birkey et al. (2021), and at 100 km in the eastern path. The X-Ds under the LAB are seen in the range  
396 from 250 to 300 km, consistent with the depths identified by Taira and Yoshizawa (2020) at 270 km and the Lehmann  
397 discontinuity by Revenaugh and Jordan (1991) at around 255–280 km.

#### 398 **4.2.2. WRAB station in central Australia**

399 Figure 8 shows the inversion resultants at WRAB, located in the NAC, for three event groups. Despite being  
400 located in the stable craton, WRAB, three inversion results at WRAB display clear azimuthal dependence of radially  
401 anisotropic S-wave profiles (Figure 8 (b-d)). No significant S-wave speed drops are observed, and the signature of the  
402 asthenosphere or low-velocity zone is unclear beneath WRAB. A high-velocity structure (4.7–4.8 km/s) extends from  
403 just below the Moho (around 50 km) to the deep upper mantle, with a clear increase in radial anisotropy around the  
404 LAT.

405 For WRAB, the lithosphere base is defined by increased radial anisotropy, consistent with previous tomographic  
406 studies that indicate a thick high-speed region in the southern NAC (e.g., Yoshizawa, 2014; Magrini et al., 2023;  
407 de Laat et al., 2023). Despite the absence of a clear low-velocity zone in the AusREM model (Kennett et al., 2013),  
408 anomalous radial anisotropy with  $V_{SH} > V_{SV}$  (Yoshizawa, 2014; Yoshizawa and Kennett, 2015) and the alignment of  
409 azimuthal anisotropy with plate motion direction (e.g., Simons et al., 2002; Fishwick et al., 2008; de Laat et al., 2023)  
410 suggest that the horizontal shear flow in the ductile asthenosphere drives the fast motion of the Australian plate. Thus,  
411 defining the lithosphere base via radial anisotropy can be a reasonable criterion.

412 The estimated lithosphere base from the increased radial anisotropy for WRAB varies with the incoming P-wave  
413 directions: the western path indicates a thicker lithosphere of about 180 km, while the northern and eastern paths  
414 show a thinner lithosphere of about 120–130 km. X-Ds are detected at around 300 km, at which radial anisotropy  
415 is weakened and approaches isotropy ( $SH \approx SV$ ). In the lithospheric depth, we can identify minor S-wave velocity  
416 changes at 70–80 km depth in the northern and eastern paths, equivalent to MLD depths inferred from S-RFs (Birkey

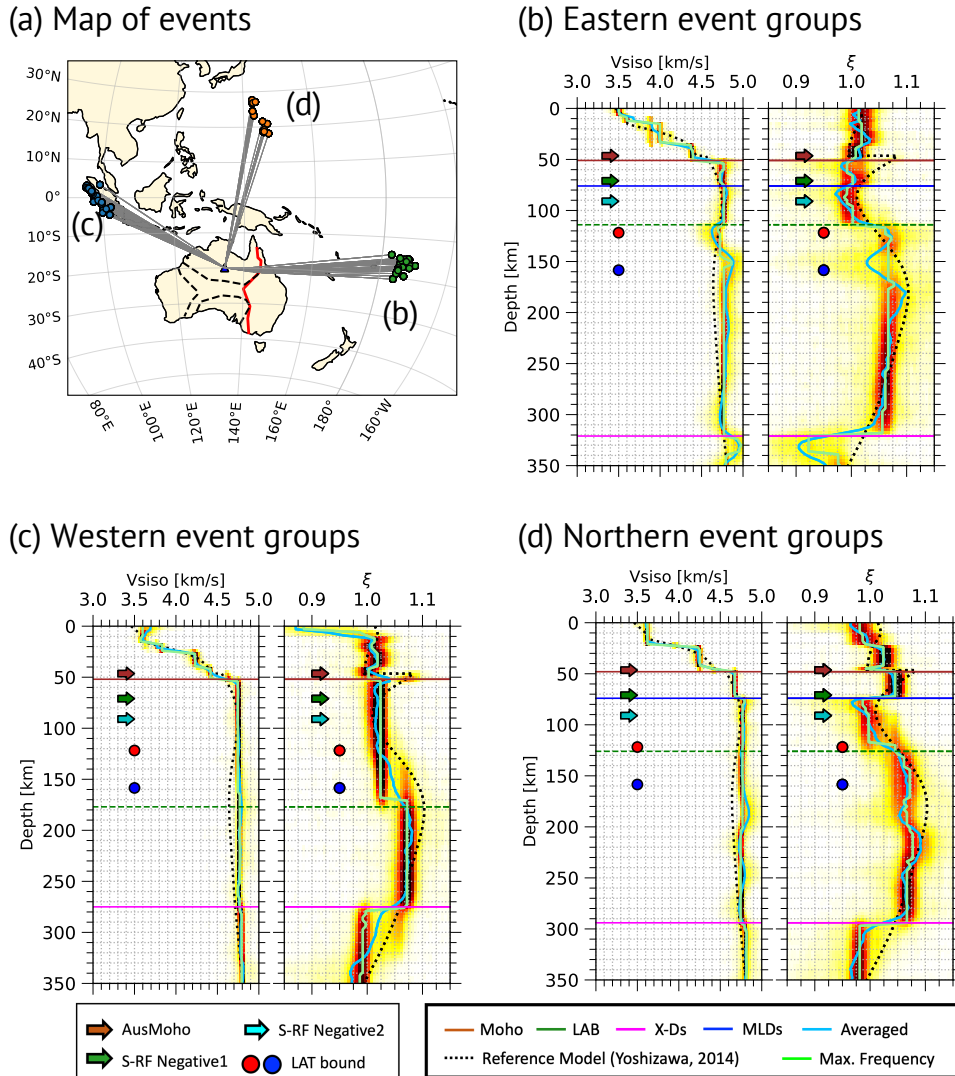


**Figure 8:** Same as Figure 5, but for II.WRAB. The horizontal green dashed lines represent the estimated base of the lithosphere (relevant to LAB but identified based on radial anisotropy).

et al., 2021). However, our models show a positive velocity jump with decreasing anisotropy, contrasting with earlier MLD observations from S-RFs (Ford et al., 2010; Birkey et al., 2021).

## 5. Localized conversion point maps

After gathering Ps conversion depths for each discontinuity in the 1-D profiles, we created conversion point (CP) maps to visualize lateral variations of Ps-conversion depths around each station, representing the spatial distribution of seismic discontinuity. This approach is similar to Ford et al. (2010) with S-RFs, in which S-to-P conversion points tend to be distant from the station ( $\approx 250$ – $350$  km at 200 km depth). Our P-RF datasets provide the P-to-S conversion points within 100–150 km around the station, enabling more localized mapping of each discontinuity.

425 To estimate CP maps, at first, we constructed a local reference 1-D shear velocity model for each station from the  
426 average of the mode (maximum frequency) models for azimuth-dependent 1-D S-wave profiles (e.g., green lines in  
427 Figures 5, 6, 7 and 8). The P-wave structure is derived from the scaling of the S-wave based on AK135 (Kennett et al.,  
428 1995) as in the inversion. Then, the local 1-D reference model is used to compute ray paths to estimate the lateral  
429 locations of the Ps conversion points for the azimuth-dependent boundary depths explained in the previous section. To  
430 quantify the uncertainties of our depth estimations, we employed interquartile ranges (IQR) for each discontinuity depth  
431 from the ensemble solutions, as the resultant probabilistic densities do not always follow the Gaussian distribution.

432 Resultant CP maps and their depth uncertainties are shown in Figures 9 and 10 for two Phanerozoic stations and  
433 Figures 11 and 12 for three cratonic stations, including Moho, MLDs, LAB, and X-Ds. In this section, we investigate  
434 the spatial distribution of seismic discontinuities around each station based on these CP maps.

## 435 **5.1. Phanerozoic eastern Australia**

436 Figures 9 and 10 show CP maps and uncertainties (derived from IQR) for the Moho, LAB, and X-Ds around CTAO  
437 and CAN stations. Due to the limitations of event distributions, southern areas for both stations are unsampled, so we  
438 focus on the northwestern, northern, and eastern CPs. The IQR for the Moho are small ( $\approx 3$  km), while those for deeper  
439 interfaces are relatively large ( $\approx 10$  km).

### 440 **5.1.1. Moho, LAB, and X-Ds in eastern Australia**

441 For the Moho, CP depths (left panels in Figure 9) exhibit almost no significant azimuthal dependence at both  
442 stations, suggesting a nearly consistent crustal thickness. Around CAN, our results reflect somewhat shallower northern  
443 Moho depths, aligning with Kennett et al. (2023). Similarly, CTAO shows a nearly constant Moho depth at around 40  
444 km.

445 In contrast, the CP maps of the LAB (middle panels in Figure 9) reveal distinct images for each station, consistent  
446 with inversion results (Figures 5 and 6). At CTAO, LAB depths increase from east to west, with the depth ranging  
447 from 70 km to 120–130 km, supporting a stepwise lithospheric thickening at the eastern continental margin (Fishwick  
448 et al., 2008) and the rapid deepening of the LAT upper bound to the northwest of CTAO (Yoshizawa, 2014). At CAN,  
449 however, the LAB depth remains consistent at 65–80 km, suggesting stable lithospheric thickness to the north, as seen  
450 in previous models (Fishwick et al., 2008). Also, S-wave reductions are more pronounced at CAN, as observed in the  
451 tomography model by Yoshizawa (2014).

452 The CP maps of X-Ds (right panels in Figure 9) indicate multiple interfaces with positive shear wave speed jumps  
453 clustered around 170 km, 250 km, and 310 km. The shear wave speed changes across these interfaces are smaller than  
454 those across the LAB, likely undetectable by long-wavelength surface waves only. In the similar depth ranges, Taira  
455 and Yoshizawa (2020) identified two interfaces at 230–240 km and 300–310 km, and Revenaugh and Jordan (1991)

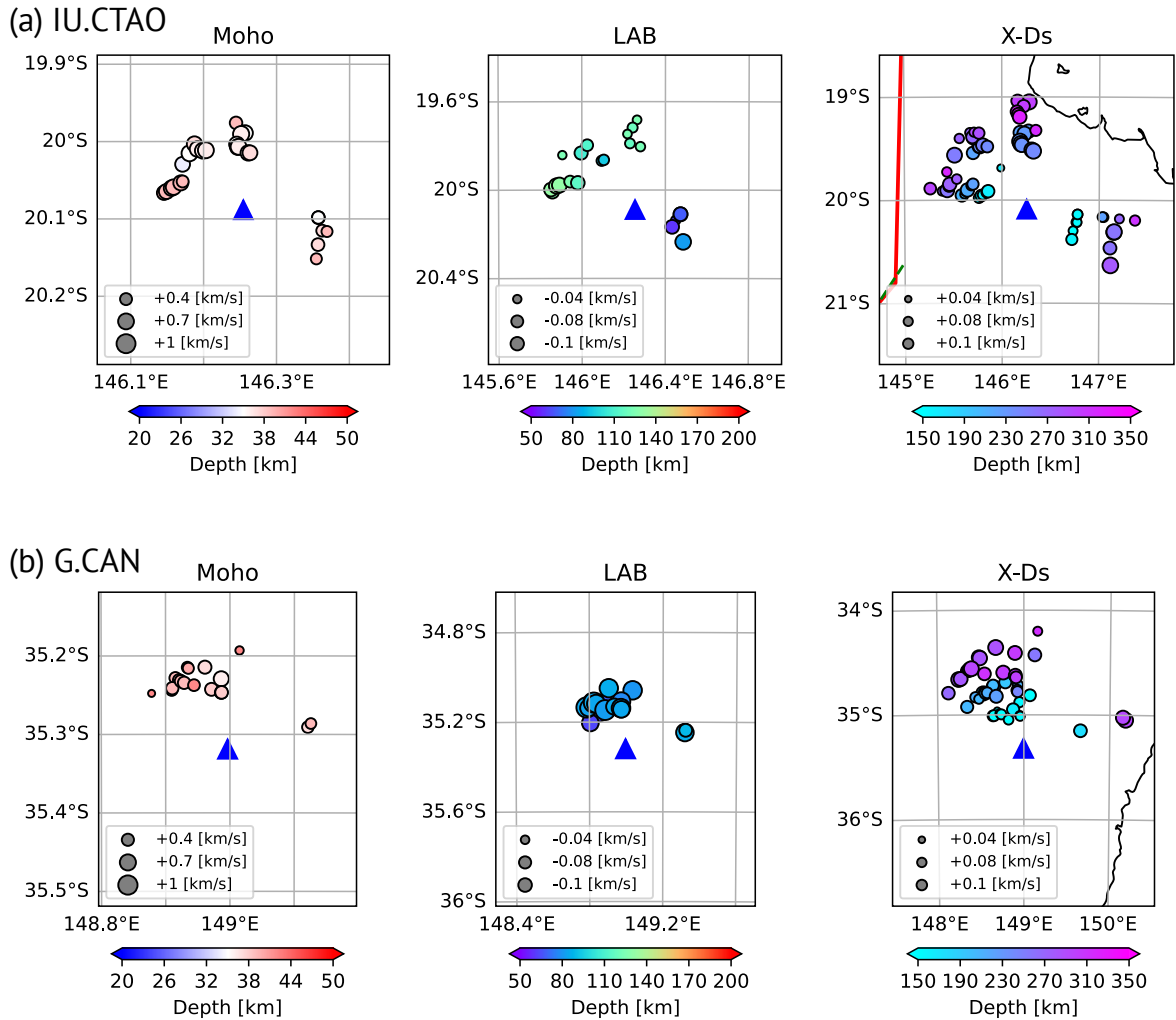


**Figure 9:** Conversion points (CPs) maps for Moho, LAB, and X-Ds at two stations in eastern Australia: (a) IU.CTAO and (b) G.CAN. For each station, the CP maps for Moho, LAB, and X-Ds are shown from left to right. A red line in the rightmost panel of (a) indicates the Tasman line. Blue triangles on all maps represent the station locations. Circles indicate the inferred Ps conversion locations, with color and size representing the depth and magnitude of the shear wave velocity across the interface.

456 also detected two interfaces at 180–220 km (the Lehmann discontinuity) and around 330 km (X-D), although our CP  
 457 maps for X-Ds suggest three or four distinct interfaces beneath the LAB.

## 458 5.2. Cratonic central and western Australia

459 Figure 11 displays CPs from the Moho, MLDs, LAB (or lithospheric base), and X-Ds at MBWA, NWAO, and  
 460 WRAB stations, and Figure 12 shows the uncertainties of discontinuity depths based on IQR. Note that, unlike Figure  
 461 9 for stations in eastern Australia, where MLD is generally unclear, we add the MLD's CP map in Figure 11 in the mid-  
 462 left panels, with circles and crosses indicating negative and positive S-wave speed changes, respectively. For WRAB,  
 463 the mid-right panel represents the lithospheric thickness estimated from radial anisotropy as described in Section 4.2.2.

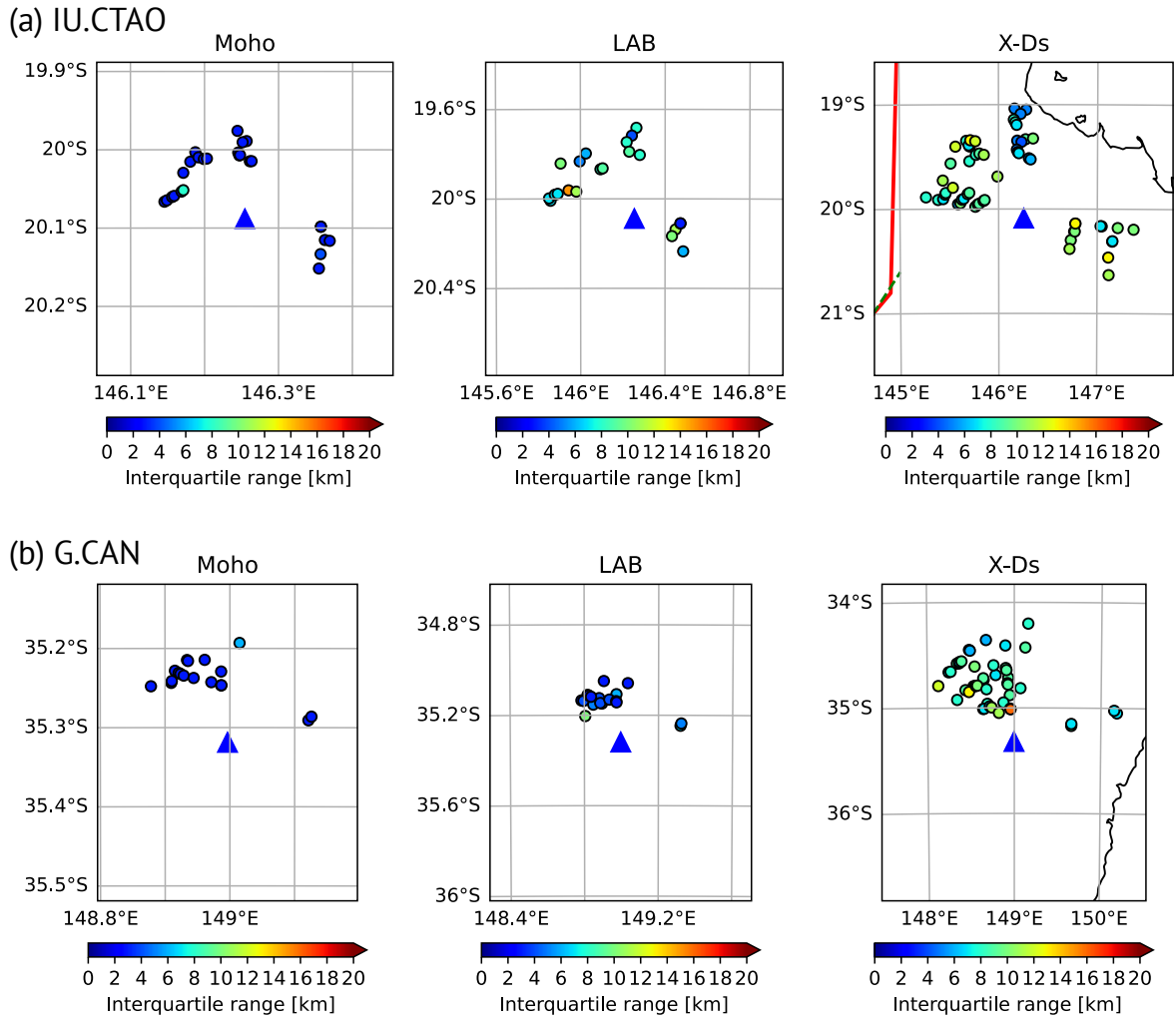


**Figure 10:** Depth uncertainties of conversion depths for Moho, LAB, and X-Ds: (a) IU.CTAO and (b) G.CAN. Circles are the location of conversion points, with colors indicating the interquartile ranges.

464 Except for the lithospheric base beneath WRAB, Figure 12 exhibits the IQRs for the upper mantle discontinuities  
 465 (MLD, LAB, and X-Ds) are generally around 10–15 km, which are greater than those in the eastern Phanerozoic area  
 466 (Figure 10). Larger uncertainties in the LAB depth possibly reflect the ambiguous transition from the lithosphere to  
 467 the asthenosphere under the cratonic areas (e.g., Yoshizawa, 2014). Besides, the lithospheric base under WRAB shows  
 468 larger IQRs than the other two cratonic stations, MBWA and NWA0 (Figure 12). These results are expected from  
 469 the somewhat ambiguous definition of the lithospheric base using radial anisotropy since the horizontally polarized S  
 470 velocity ( $V_{SH}$ ) cannot be constrained by the receiver functions.

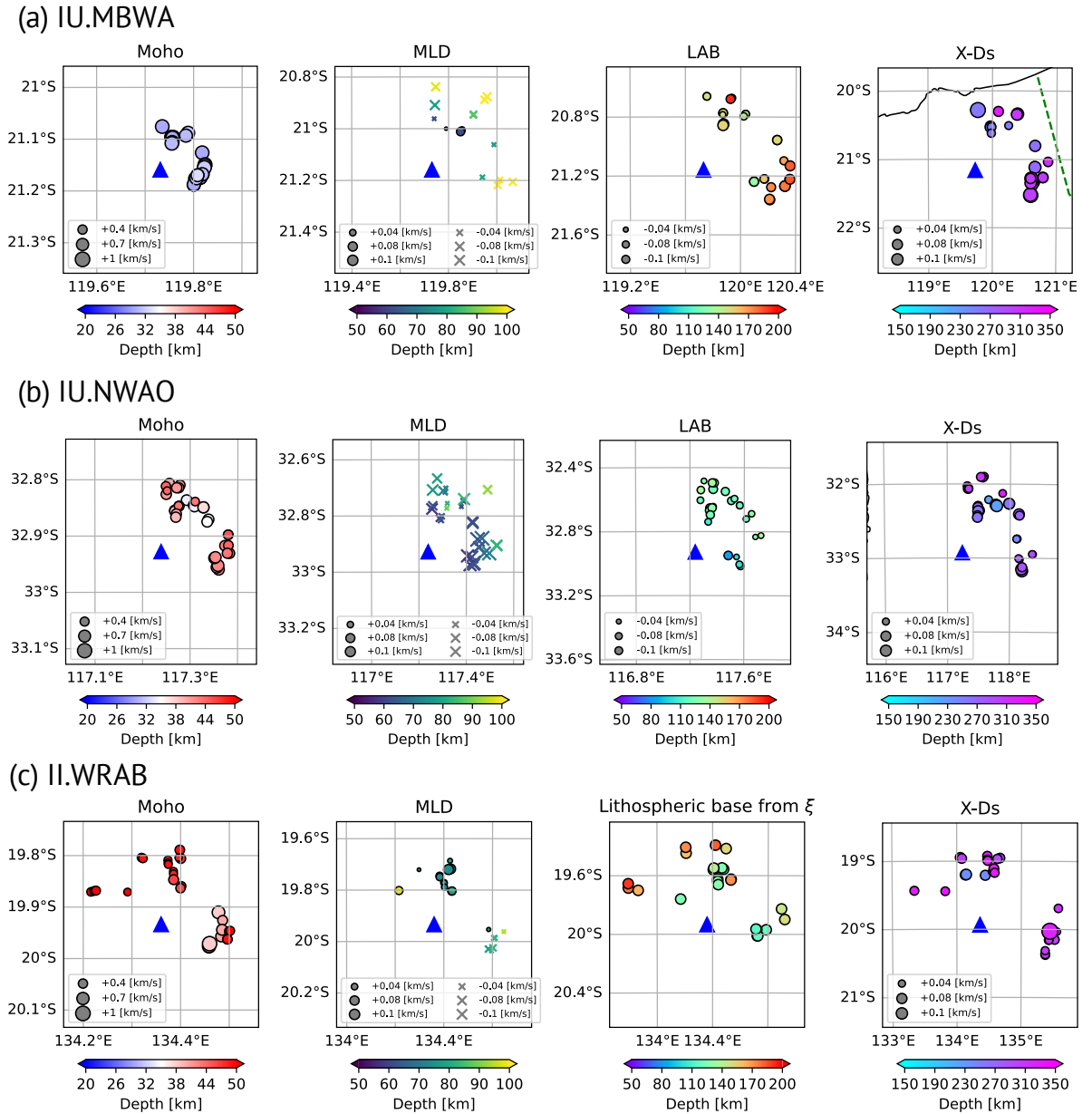


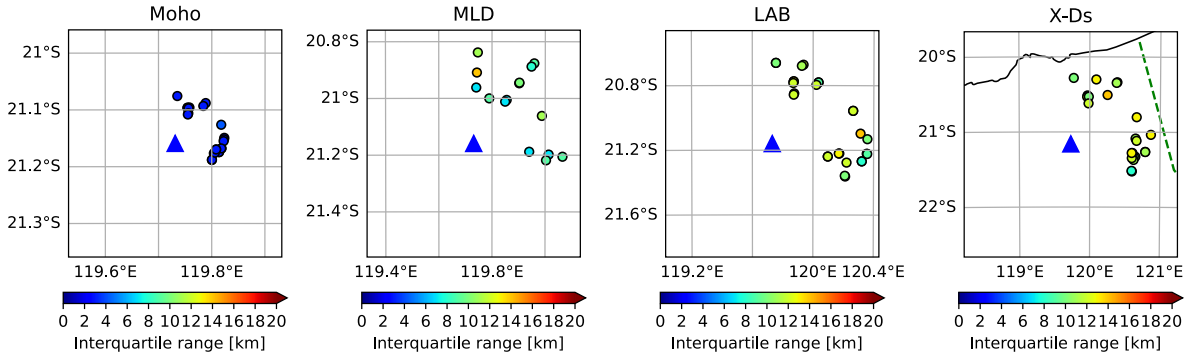
**Figure 11:** Same as Figure 9, but for three cratonic stations where MLDs have been observed: (a) IU.MBWA, (b) IU.NWAO, and (c) II.WRAB. CP maps for MLDs are added to the mid-left panel in all stations. Note that the mid-right panel for (c) II.WRAB represents the lithospheric base derived from an increase of radial anisotropy  $\xi$ , for which the circle sizes are constant, unlike other panels. The mid-left panel displays the CPs for MLDs, with circles and crosses indicating negative and positive changes in shear velocity, respectively.

### 471 5.2.1. Moho, LAB, and X-Ds in cratonic regions

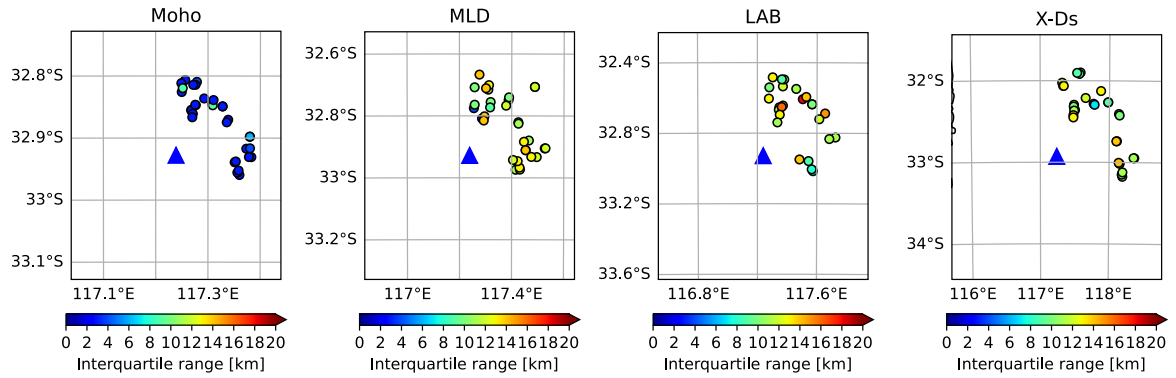
472 For the Moho, CP maps at MBWA and NWAO are almost azimuth-independent, but WRAB shows varying depths  
 473 of about 10 km between the north and east (leftmost panels in Figure 11 (a-c)). This variation, also seen in array-based  
 474 P-RF studies (Sippl, 2016) and in our P-RF data (Figure 3 and S5), suggests changes in Moho geometry around WRAB.

Lateral changes in the upper mantle discontinuities

(a) IU.MBWA



(b) IU.NWAO



(c) II.WRAB

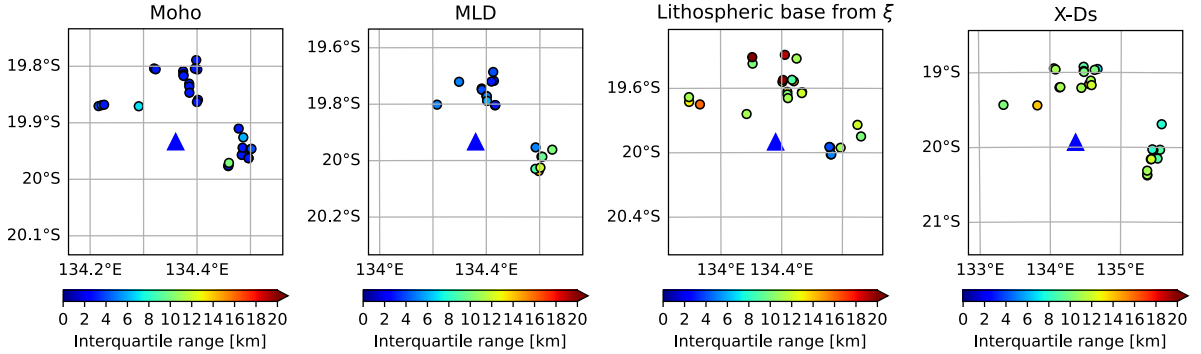


Figure 12: Same as Figure 10. As in Figure 11, the interquartile ranges of MLDs are shown here.

475 The LAB/lithosphere base shows clear azimuthal trends, especially at MBWA and WRAB. At MBWA, the LAB  
 476 deepens westward from 140–150 km to 170 km depth, possibly reflecting the structural transition near the tectonic  
 477 margin between the Pilbara craton and the suture zone. At NWAO, the LAB appears to deepen slightly from the south  
 478 (100–110 km) to the north (130 km), consistent with previous models (Kennett et al., 2013; Yoshizawa, 2014; Magrini  
 479 et al., 2023). Comparing the two stations in the WAC, the velocity change at MBWA is likely more pronounced than  
 480 at NWAO (Figure 11 (a, b)). For WRAB, where lithospheric base depths are inferred from radial anisotropy, the

481 lithospheric thickness varies from 120-140 km in the southeast to about 180 km in the northwest (Figure 11 (c)),  
482 consistent with the LAB model from fundamental-mode surface waves (Magrini et al., 2023). The upper limit of the  
483 LAT derived from the multimode surface waves (Yoshizawa, 2014) indicate that WRAB is located at the transition  
484 between the shallow and deep LAT regions. Our results may reflect such lateral heterogeneity in the upper mantle  
485 structure.

486 The CP maps for X-Ds, associated with positive velocity changes and weaker radial anisotropy, show less azimuthal  
487 dependence than the LAB or the lithospheric base at all three stations (right panels in Figure 11). While we did not  
488 detect localized X-D variations, CP depths indicate two distinct depths for each station: 260 km and 300–310 km for  
489 MBWA, 220 km and 270–290 km for NWA0, and 240 km and 320 km for WRAB. The shallower depth at MBWA  
490 is equivalent to the Lehmann discontinuity identified by Taira and Yoshizawa (2020), though we did not observe an  
491 interface at 200 km as reported by Drummond et al. (1982). Besides, the deeper interface at 300 km has not been  
492 reported previously. At NWA0, the deeper depth matches observations in Revenaugh and Jordan (1991), while the  
493 shallower one has not been reported. For WRAB, our CP map for X-Ds cluster below 300 km depths, with a previously  
494 unreported discontinuity around 230–240 km (Figure 11 (c)). Earlier studies using P-wave amplitudes and travel times  
495 (Hales et al., 1980; Leven, 1985) also suggested discontinuities around 200 km and 325 km beneath the NAC. Some  
496 of our X-Ds are consistent with these earlier findings, suggesting multiple interfaces are present. Extended spatial  
497 mapping with more stations will be essential for further investigating the X-Ds (or Lehmann discontinuity).

### 498 **5.2.2. MLDs in cratonic regions**

499 The CPs of MLDs beneath MBWA and NWA0 show shear wave speed reductions at multiple depths within the  
500 lithosphere (Figure 11), consistent with earlier studies (Ford et al., 2010; Sun et al., 2018; Taira and Yoshizawa, 2020;  
501 Birkey et al., 2021). At MBWA, smaller samples show the shear wave speed jumps at 60 km, possibly related to  
502 shallower positive S-RF phases indicated by Birkey et al. (2021).

503 On the contrary, MLDs at WRAB exhibit unique characteristics (mid-left panel in Figure 11 (c)). In the east, shear  
504 wave speed reductions at 80–90 km are consistent with negative MLDs detected in S-RF and joint inversion studies  
505 (Ford et al., 2010; Birkey et al., 2021; Taira and Yoshizawa, 2020). The earlier inversion study by Taira and Yoshizawa  
506 (2020) mainly used events from the Tonga-Kermadec Trench, detecting the negative MLDs at 80 km, which matches  
507 our results in the east of WRAB. In the north, however, we observe increased S-wave speeds at 70–80 km, aligning  
508 with classical studies that detected a positive velocity step at around 75 km in the NAC using the events from the Banda  
509 Sea, equivalent to the Hales discontinuity (Hales et al., 1980). This contrasts with negative MLDs found in S-RFs for  
510 the northern piercing points (Ford et al., 2010), possibly due to the intrinsic differences between P-RFs and S-RFs,  
511 such as conversion points, incident angles, and wavelength.

512 An alternative explanation may involve vertical variations in azimuthal anisotropy. Selway et al. (2015) suggested  
 513 MLDs in RFs could result from azimuthal anisotropic layering through simple forward modeling of RFs. Similarly,  
 514 Chen et al. (2021) and Birkey and Ford (2023) discussed the link between the depths of MLDs and vertical changes  
 515 in azimuthal anisotropy, using azimuth-dependent radial and transverse P-RFs in Australian cratons. Around WRAB,  
 516 layered azimuthal anisotropy has been imaged by surface wave tomography (Simons et al., 2002; Debayle et al., 2005;  
 517 de Laat et al., 2023). Incorporating azimuthal anisotropy in our joint inversion methods of P-RFs and SWDs will  
 518 provide additional constraints on the nature of MLDs, though it is beyond the scope of the current study.

519 Although our dataset does not involve azimuthal anisotropy, it includes multimode Love and Rayleigh wave  
 520 dispersions in addition to P-RFs, allowing us to analyze radial anisotropy across MLDs. Yoshizawa and Kennett (2015)  
 521 compared their radially anisotropic S-wave model derived from the multimode SWDs and S-RFs by Ford et al. (2010),  
 522 suggesting that the MLDs may be linked to the vertical changes (weakening) of radial anisotropy. Subsequent studies  
 523 proposed that MLDs may involve multiple interfaces (Sun et al., 2018; Taira and Yoshizawa, 2020; Chen et al., 2021;  
 524 Birkey et al., 2021), though the relationship between MLDs and radial anisotropy  $\xi$  remains unclear.

525 To investigate this point, we examined the vertical gradient signs of  $\xi$  across MLDs in Figure 13, excluding CPs with  
 526 change smaller than 1 %. The resultant CP maps in (Figure 13) reveal distinct patterns by station. At MBWA, shallower  
 527 MLDs show a decrease in  $\xi$ , while deeper interfaces indicate increasing anisotropy (Figure 13 (a)). At NWAO, shallow  
 528 eastern MLDs ( $\approx 60$  km) show increasing  $\xi$ , while deeper MLDs (70–80 km) show a decrease (Figure 13 (b)). At  
 529 WRAB, azimuthal dependency aligns with S-wave speed changes (Figure 13 (c)): positive speed changes coincide  
 530 with weakened radial anisotropy and vice versa. Although the localized CPs do not fully clarify the nature of multiple  
 531 MLDs, these new findings may contribute to understanding the origins of MLDs.

## 532 6. Discussion

533 To validate our approach of estimating localized conversion depths using azimuth-dependent radial P-RFs, we plot  
 534 the estimated conversion points at CTAO, CAN, and WRAB on the E-W cross sections of the tomography model from  
 535 Yoshizawa (2014) in Figure 14. Since the employed events are mostly distributed in a limited range from the northwest  
 536 to the east of Australia, we lack CP samples in the south of all stations. We selected three stations (CTAO, CAN, and  
 537 WRAB), for which nearly 180° in back-azimuth is covered, excluding MBWA and NWAO to avoid biases due to very  
 538 limited azimuthal coverage (about 90°).

539 Figure 14 compares our estimated CPs for MLDs, LAB, and X-Ds with the surface-wave tomography models  
 540 (Yoshizawa, 2014) with depth uncertainties estimated from the IQRs for each discontinuity. Projected conversion  
 541 points (CPs) are located within 70 km of each station. The background contours display isotropic S-wave speed in  
 542 the top panels and radial anisotropy in the bottom.

Lateral changes in the upper mantle discontinuities

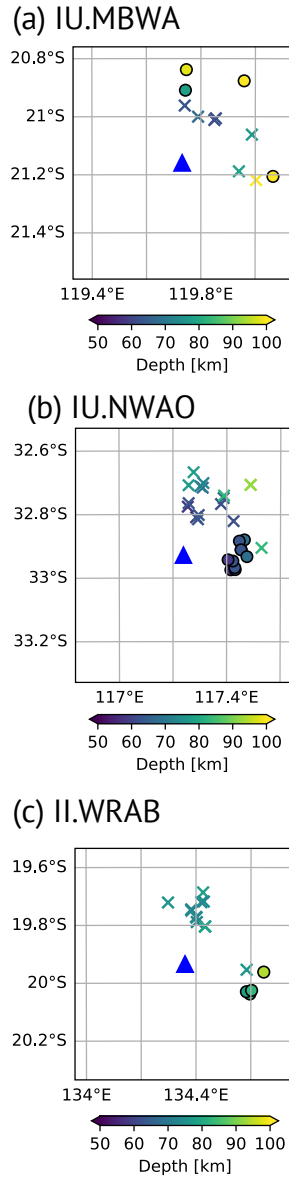


**Figure 13:** The vertical change in radial anisotropy ( $> 1\%$ ) across the MLDs at (a) IU.MBWA, (b) IU.NWAO, and (c) II.WRAB. Blue triangles represent station locations. Colored symbols denote the conversion points, with color indicating depth. Circles and crosses denote positive and negative changes in radial anisotropy  $\xi$  with depth, respectively.

543 The LAB (or the lithospheric base) CPs are located at the transition to a relatively lower-velocity zone, particularly  
 544 evident at CTAO and CAN (Figure 14). Beneath CTAO, our estimates closely match the lateral change in the low-  
 545 velocity zone. For WRAB, the lithospheric base is situated within a low-velocity zone relative to the surrounding area,  
 546 supporting our definition based on radial anisotropy can be reasonable in the southern NAC. These LAB CP depths  
 547 generally align with the regions of intense radial anisotropy, reflecting the asthenospheric shear flow. Thus, our local  
 548 CP maps effectively capture the lateral variations of lithospheric thickness.

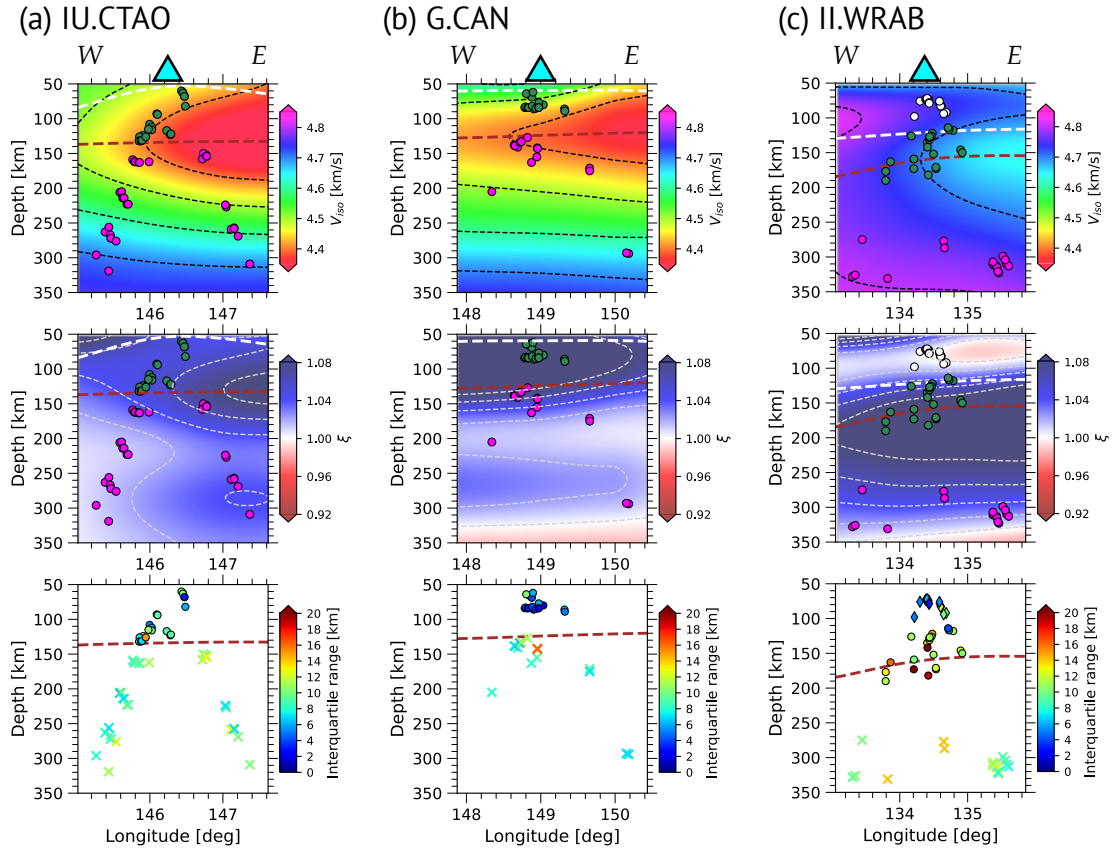


**Figure 14:** Comparison of conversion points from this study with E-W cross-section of the isotropic S-wave speed (top panels) and radial anisotropy (middle panels) models by Yoshizawa (2014), and interquartile ranges (bottom panels): (a) IU.CTAO, (b) G.CAN, and (c) II.WRAB. Cyan triangles show station locations. White and red thick dashed lines indicate the upper and lower bounds of the LAT (Yoshizawa, 2014). Black and white thin dashed lines represent shear wave speed contours of 0.1 km/s and the radial anisotropy of 0.04. White, green, and magenta dots denote conversion points for the MLDs, lithospheric base, and X-Ds, respectively. For bottom panels, circles, crosses, and diamonds represent IQR-based uncertainties for the LAB (or lithospheric base), X-Ds, and MLDs, respectively.

549 The X-D CPs, associated with S-wave velocity increases, coincide with weakened radial anisotropy, which is  
 550 consistent with characteristics of the Lehmann discontinuity (L-D) as previously described (e.g., Gaherty and Jordan,  
 551 1995; Thybo, 2006; Calò et al., 2016; Taira and Yoshizawa, 2020), suggesting a transition from dislocation to diffusion  
 552 creep across the L-D (Karato, 1992). Although our CPs for X-Ds are observed at multiple depths with varied agreement  
 553 to previous studies, they likely correspond to the L-D as the base of the anisotropic layer (Gaherty and Jordan, 1995;  
 554 Karato, 1992). Furthermore, our detected X-D depths form some clusters at specific depths, consistent with earlier  
 555 studies (Hales et al., 1980; Leven, 1985; Revenaugh and Jordan, 1991; Taira and Yoshizawa, 2020), suggesting multiple  
 556 interfaces below the LAB. These CPs contribute to understanding large-scale X-D distributions, which could further  
 557 illuminate the origins of these interfaces when combined with other geophysical insights, such as the phase transitions  
 558 of constituent minerals.

559 In Figure 14 (c) at WRAB, MLDs are observed at multiple depths from 60–90 km, where the S-wave velocity is  
560 notably high ( $\approx 4.75$  km/s), with weak velocity changes in the uppermost mantle beneath the station. The tomographic  
561 S-wave model in Figure 14 (c) shows a positive velocity gradient in these depths, matching the MLDs north of WRAB  
562 (around 70 km depth), characterized by positive velocity jumps in our observation (Figure 11 (c)). In contrast, the  
563 MLDs east of WRAB (around 80 km depth) appear near a relatively lower-velocity zone extending to the LAT, likely  
564 corresponding to negative S-RF peaks.

565 Some earlier S-RF studies have suggested negative peaks at MLD depths (Birkey et al., 2021), suggesting shear  
566 velocity reduction, where positive velocity jumps are detected in the north of WARB in our study. One possible  
567 explanation is the influence of azimuthal anisotropy, which our current study did not consider but can be a topic  
568 of future work. In addition, MLDs identified in both S-RF studies and our model may be related to reductions in  
569 radial anisotropy within the lithosphere (Figures 13 and 14; Yoshizawa and Kennett, 2015; Taira and Yoshizawa,  
570 2020). Recent azimuthal anisotropy model also indicates rapid fast-axis changes at the MLD depths (de Laat et al.,  
571 2023), suggesting that some MLDs may reflect changes in anisotropic properties, which can also be evident from the  
572 azimuth-dependent transverse P-RFs (Birkey and Ford, 2023).

573 Moreover, the MLD characteristics appear to vary by tectonic province, likely due to distinct ancient tectonic events  
574 in each craton. Applying our joint inversion approach to more stations across Australia will allow us to better map MLD  
575 distribution and elastic properties, providing further insights into these regional differences.

## 576 7. Conclusions

577 In this study, we introduced a new approach using azimuth-dependent P-wave receiver functions (P-RFs) in the  
578 framework of joint Bayesian inversions with multimode surface wave data. Azimuthal variations in P-RFs generally  
579 indicate lateral changes in seismic interfaces or anisotropic layering beneath a station. Based on the posterior of local  
580 1-D profiles, we estimated the major seismic interfaces in the upper mantle, which led to the construction of conversion  
581 point maps for each discontinuity.

582 Through analysis of five permanent stations, we identified some notable characteristics of upper mantle disconti-  
583 nuities beneath Australia, which can be summarized as follows:

- 584 1. Beneath CTAO in northeastern Australia, the lithosphere-asthenosphere boundary (LAB) deepens sharply from  
585  $\sim 70$  km in the east to 120–130 km toward the west and north. In contrast, the LAB under CAN is nearly flat at  
586  $\sim 80$  km.
- 587 2. In the stable craton of western Australia, the LAB depth varies laterally, though more gradually than in the  
588 eastern Phanerozoic region.

- 589 3. Australian X-discontinuities (X-Ds) beneath the LAB appear at three to four distinct depths, indicating multiple  
590 interfaces with weakened radial anisotropy.
- 591 4. MLDs consist of multiple interfaces at varying lithospheric depths, with different elastic properties by location.  
592 In particular, MLDs beneath WRAB include shallower positive discontinuities previously unreported in  
593 Australian S-RF studies.

594 Due to the limitations of our data set to five permanent stations, the spatial distributions of upper mantle  
595 discontinuities remain unconstrained. In future work, we plan to incorporate all the available permanent and temporary  
596 stations across Australia to construct a comprehensive map of the lithosphere, MLDs, and X-discontinuities beneath  
597 the LAB using our approach proposed in this study. This mapping will clarify continental-wide distributions and the  
598 seismological nature of each discontinuity, deepening our understanding of Australia's ancient and present tectonics.

## 599 Acknowledgments

600 We downloaded all seismograms used in this study from the IRIS Data Management Center (<https://ds.iris.edu/ds/nodes/dmc/>)  
601 This study was partly supported by JST SPRING grant number JPMJSP2119 to KT and JSPS KAKENHI (grant number  
602 24KJ0294 to KT; 20K04096 and 23K03539 to KY). We used ObsPy (Beyreuther et al., 2010) for downloading and  
603 analyzing all seismic waveform data. We used matplotlib (Hunter, 2007), cartopy (Office, 2010), Generic Mapping  
604 Tools (Wessel et al., 2019), and PyGMT (Uieda et al., 2021) to create figures. We thank Toru Taira for sharing his  
605 original trans-dimensional Bayesian inversion codes, which were helpful during the development of methods in this  
606 study. This study was partly achieved through the use of the supercomputer system at the information initiative center,  
607 Hokkaido University.

## 608 Data Availability

609 All the seismograms used in this study can be available from the IRIS Data Management Center (<https://ds.iris.edu/ds/nodes/d>)

## 610 CRediT authorship contribution statement

611 **Kotaro Tarumi:** Conceptualization, Data curation, Methodology, Formal analysis, Funding acquisition, Inves-  
612 tigation, Visualization, Software, Writing - Original draft. **Kazunori Yoshizawa:** Conceptualization, Data curation,  
613 Methodology, Funding acquisition, Investigation, Supervision, Project Administration, Writing – review and editing.

## 614 References

615 Abt, D.L., Fischer, K.M., French, S.W., Ford, H.A., Yuan, H., Romanowicz, B., 2010. North American lithospheric discontinuity structure imaged  
616 by Ps and Sp receiver functions. *Journal of Geophysical Research: Solid Earth* (1978–2012) 115. doi:10.1029/2009jb006914.

## Lateral changes in the upper mantle discontinuities

- 617 Ai, S., Akuhara, T., Morishige, M., Yoshizawa, K., Shinohara, M., Nakahigashi, K., 2023. Layered Evolution of the Oceanic Lithosphere Beneath  
618 the Japan Basin, the Sea of Japan. *Journal of Geophysical Research: Solid Earth* 128. doi:10.1029/2022jb025581.
- 619 Akuhara, T., Nakahigashi, K., Shinohara, M., Yamada, T., Shiobara, H., Yamashita, Y., Mochizuki, K., Uehira, K., 2021. Lithosphere–asthenosphere  
620 boundary beneath the Sea of Japan from transdimensional inversion of S-receiver functions. *Earth, Planets and Space* 73, 171. doi:10.1186/  
621 s40623-021-01501-5.
- 622 Argus, D.F., Gordon, R.G., DeMets, C., 2011. Geologically current motion of 56 plates relative to the no-net-rotation reference frame. *Geochemistry,  
623 Geophysics, Geosystems* 12, n/a–n/a. doi:10.1029/2011gc003751.
- 624 Beyreuther, M., Barsch, R., Krischer, L., Megies, T., Behr, Y., Wassermann, J., 2010. ObsPy: A Python Toolbox for Seismology. *Seismological  
625 Research Letters* 81, 530–533. doi:10.1785/gssrl.81.3.530.
- 626 Bianchi, I., Park, J., Agostinetti, N.P., Levin, V., 2010. Mapping seismic anisotropy using harmonic decomposition of receiver functions: An  
627 application to Northern Apennines, Italy. *Journal of Geophysical Research: Solid Earth* 115. doi:10.1029/2009jb007061.
- 628 Birkey, A., Ford, H.A., 2023. Anisotropic structure of the Australian continent. *Frontiers in Earth Science* 10, 1055480. doi:10.3389/feart.  
629 2022.1055480.
- 630 Birkey, A., Ford, H.A., Dabney, P., Goldhagen, G., 2021. The Lithospheric Architecture of Australia From Seismic Receiver Functions. *Journal of  
631 Geophysical Research: Solid Earth* 126. doi:10.1029/2020jb020999.
- 632 Bodin, T., Leiva, J., Romanowicz, B., Maupin, V., Yuan, H., 2016. Imaging anisotropic layering with Bayesian inversion of multiple data types.  
633 *Geophysical Journal International* 206, 605–629. doi:10.1093/gji/ggw124.
- 634 Bodin, T., Sambridge, M., Tkalčić, H., Arroucau, P., Gallagher, K., Rawlinson, N., 2012. Transdimensional inversion of receiver functions and  
635 surface wave dispersion. *Journal of Geophysical Research: Solid Earth (1978–2012)* 117, n/a–n/a. doi:10.1029/2011jb008560.
- 636 Bodin, T., Yuan, H., Romanowicz, B., 2014. Inversion of receiver functions without deconvolution—application to the Indian craton. *Geophysical  
637 Journal International* 196, 1025–1033. doi:10.1093/gji/ggt431.
- 638 Calò, M., Bodin, T., Romanowicz, B., 2016. Layered structure in the upper mantle across North America from joint inversion of long and short  
639 period seismic data. *Earth and Planetary Science Letters* 449, 164–175. doi:10.1016/j.epsl.2016.05.054.
- 640 Chen, X., Levin, V., Yuan, H., Klaser, M., Li, Y., 2021. Seismic Anisotropic Layering in the Yilgarn and Superior Cratonic Lithosphere. *Journal of  
641 Geophysical Research: Solid Earth* 126. doi:10.1029/2020jb021575.
- 642 Cheng, C., Bodin, T., Tauzin, B., Allen, R.M., 2017. Cascadia subduction slab heterogeneity revealed by three-dimensional receiver function  
643 Kirchhoff migration. *Geophysical Research Letters* 44, 694–701. doi:10.1002/2016gl072142.
- 644 Davies, D.R., Rawlinson, N., Iaffaldano, G., Campbell, I.H., 2015. Lithospheric controls on magma composition along Earth’s longest continental  
645 hotspot track. *Nature* 525, 511–514. doi:10.1038/nature14903.
- 646 Debayle, E., Kennett, B., Priestley, K., 2005. Global azimuthal seismic anisotropy and the unique plate-motion deformation of Australia. *Nature*  
647 433, 509–512. doi:10.1038/nature03247.
- 648 Debayle, E., Kennett, B.L.N., 2000. The Australian continental upper mantle: Structure and deformation inferred from surface waves. *Journal of  
649 Geophysical Research: Solid Earth* 105, 25423–25450. doi:10.1029/2000jb900212.
- 650 de Laat, J.I., Lebedev, S., Celli, N.L., Bonadio, R., Chagas de Melo, B., Rawlinson, N., 2023. Structure and evolution of the Australian  
651 plate and underlying upper mantle from waveform tomography with massive data sets. *Geophysical Journal International* 234, 153–189.  
652 doi:10.1093/gji/ggad062.
- 653 Drummond, B.J., Muirhead, K.J., Hales, A.L., 1982. Evidence for a seismic discontinuity near 200km depth under a continental margin. *Geophysical  
654 Journal International* 70, 67–77. doi:10.1111/j.1365-246x.1982.tb06392.x.

## Lateral changes in the upper mantle discontinuities

- 655 Dziewonski, A.M., Anderson, D.L., 1981. Preliminary reference Earth model. *Physics of the Earth and Planetary Interiors* 25, 297–356.  
656 doi:10.1016/0031-9201(81)90046-7.
- 657 Dziewonski, A.M., Chou, T., Woodhouse, J.H., 1981. Determination of earthquake source parameters from waveform data for studies of global and  
658 regional seismicity. *Journal of Geophysical Research: Solid Earth* 86, 2825–2852. doi:10.1029/jb086ib04p02825.
- 659 Ekström, G., Nettles, M., Dziewoński, A., 2012. The global CMT project 2004–2010: Centroid-moment tensors for 13,017 earthquakes. *Physics*  
660 *of the Earth and Planetary Interiors* 200, 1–9. doi:10.1016/j.pepi.2012.04.002.
- 661 Fischer, K.M., Ford, H.A., Abt, D.L., Rychert, C.A., 2010. The Lithosphere-Asthenosphere Boundary. *Annual Review of Earth and Planetary*  
662 *Sciences* 38, 551–575. doi:10.1146/annurev-earth-040809-152438.
- 663 Fischer, K.M., Rychert, C.A., Dalton, C.A., Miller, M.S., Beghein, C., Schutt, D.L., 2020. A comparison of oceanic and continental mantle  
664 lithosphere. *Physics of the Earth and Planetary Interiors* 309, 106600. doi:10.1016/j.pepi.2020.106600.
- 665 Fishwick, S., Heintz, M., Kennett, B.L.N., Reading, A.M., Yoshizawa, K., 2008. Steps in lithospheric thickness within eastern Australia, evidence  
666 from surface wave tomography. *Tectonics* 27, n/a–n/a. doi:10.1029/2007tc002116.
- 667 Ford, H.A., Fischer, K.M., Abt, D.L., Rychert, C.A., Elkins-Tanton, L.T., 2010. The lithosphere–asthenosphere boundary and cratonic lithospheric  
668 layering beneath Australia from Sp wave imaging. *Earth and Planetary Science Letters* 300, 299–310. doi:10.1016/j.epsl.2010.10.007.
- 669 Ford, H.A., Long, M.D., Wirth, E.A., 2016. Midlithospheric discontinuities and complex anisotropic layering in the mantle lithosphere beneath the  
670 Wyoming and Superior Provinces. *Journal of Geophysical Research: Solid Earth* 121, 6675–6697. doi:10.1002/2016jb012978.
- 671 Frederiksen, A.W., Bostock, M.G., 2000. Modelling teleseismic waves in dipping anisotropic structures. *Geophysical Journal International* 141,  
672 401–412. doi:10.1046/j.1365-246x.2000.00090.x.
- 673 Frederiksen, A.W., Folsom, H., Zandt, G., 2003. Neighbourhood inversion of teleseismic Ps conversions for anisotropy and layer dip. *Geophysical*  
674 *Journal International* 155, 200–212. doi:10.1046/j.1365-246x.2003.02043.x.
- 675 Gaherty, J.B., Jordan, T.H., 1995. Lehmann Discontinuity as the Base of an Anisotropic Layer Beneath Continents. *Science* 268, 1468–1471.  
676 doi:10.1126/science.268.5216.1468.
- 677 Gilbert, H., Beck, S., Zandt, G., 2006. Lithospheric and upper mantle structure of central Chile and Argentina. *Geophysical Journal International*  
678 165, 383–398. doi:10.1111/j.1365-246x.2006.02867.x.
- 679 Green, P.J., 1995. Reversible jump Markov chain Monte Carlo computation and Bayesian model determination. *Biometrika* 82, 711–732.  
680 doi:10.1093/biomet/82.4.711.
- 681 Hales, A., Muirhead, K., Rynn, J., 1980. A compressional velocity distribution for the upper mantle. *Tectonophysics* 63, 309–348. doi:10.1016/  
682 0040-1951(80)90119-5.
- 683 Haskell, N.A., 1962. Crustal reflection of plane P and SV waves. *Journal of Geophysical Research* 67, 4751–4768. doi:10.1029/  
684 jz067i012p04751.
- 685 Hastings, W.K., 1970. Monte Carlo sampling methods using Markov chains and their applications. *Biometrika* 57, 97–109. doi:10.1093/biomet/  
686 57.1.97.
- 687 Hunter, J.D., 2007. Matplotlib: A 2D Graphics Environment. *Computing in Science & Engineering* 9, 90–95. doi:10.1109/mcse.2007.55.
- 688 Julià, J., Ammon, C.J., Herrmann, R.B., Correig, A.M., 2000. Joint inversion of receiver function and surface wave dispersion observations.  
689 *Geophysical Journal International* 143, 99–112. doi:10.1046/j.1365-246x.2000.00217.x.
- 690 Karato, S., 1992. On the Lehmann discontinuity. *Geophysical Research Letters* 19, 2255–2258. doi:10.1029/92gl02603.
- 691 Kennett, B., Yoshizawa, K., Furumura, T., 2017. Interactions of multi-scale heterogeneity in the lithosphere: Australia. *Tectonophysics* 717, 193–213.  
692 URL: <http://www.sciencedirect.com/science/article/pii/S0040195117302913>, doi:10.1016/j.tecto.2017.07.009.

- 693 Kennett, B.L.N., Engdahl, E.R., Buland, R., 1995. Constraints on seismic velocities in the Earth from traveltimes. *Geophysical Journal International*  
694 122, 108–124. doi:10.1111/j.1365-246x.1995.tb03540.x.
- 695 Kennett, B.L.N., Fichtner, A., Fishwick, S., Yoshizawa, K., 2013. Australian Seismological Reference Model (AuSREM): mantle component.  
696 *Geophysical Journal International* 192, 871–887. doi:10.1093/gji/ggs065.
- 697 Kennett, B.L.N., Gorbatov, A., Yuan, H., Agrawal, S., Murdie, R., Doublier, M.P., Eakin, C.M., Miller, M.S., Zhao, L., Czarnota, K., O'Donnell,  
698 J.P., Dentith, M., Gessner, K., 2023. Refining the Moho across the Australian continent. *Geophysical Journal International* 233, 1863–1877.  
699 doi:10.1093/gji/ggad035.
- 700 Kennett, B.L.N., Salmon, M., Saygin, E., Group, A.W., 2011. AusMoho: the variation of Moho depth in Australia. *Geophysical Journal International*  
701 187, 946–958. doi:10.1111/j.1365-246x.2011.05194.x.
- 702 Kennett, B.L.N., Sippl, C., 2018. Lithospheric discontinuities in Central Australia. *Tectonophysics* 744, 10–22. doi:10.1016/j.tecto.2018.  
703 06.008.
- 704 Kim, H., Kawakatsu, H., Akuhara, T., Shinohara, M., Shiobara, H., Sugioka, H., Takagi, R., 2021. Receiver Function Imaging of the Amphibious  
705 NE Japan Subduction Zone—Effects of Low-Velocity Sediment Layer. *Journal of Geophysical Research: Solid Earth* 126. doi:10.1029/  
706 2021jb021918.
- 707 Kim, S., Dettmer, J., Rhie, J., Tkalčić, H., 2016. Highly efficient Bayesian joint inversion for receiver-based data and its application to lithospheric  
708 structure beneath the southern Korean Peninsula. *Geophysical Journal International* 206, 328–344. doi:10.1093/gji/ggw149.
- 709 Kind, R., Mooney, W.D., Yuan, X., 2020. New insights into the structural elements of the upper mantle beneath the contiguous United States from  
710 S-to-P converted seismic waves. *Geophysical Journal International* doi:10.1093/gji/ggaa203.
- 711 Kind, R., Yuan, X., 2011. *Seismic, Receiver Function Technique*, Springer Netherlands, Dordrecht, pp. 1258–1269. URL: [https://doi.org/](https://doi.org/10.1007/978-90-481-8702-7_12)  
712 10.1007/978-90-481-8702-7\_12, doi:10.1007/978-90-481-8702-7\_12.
- 713 Kind, R., Yuan, X., Kumar, P., 2012. Seismic receiver functions and the lithosphere–asthenosphere boundary. *Tectonophysics* 536, 25–43.  
714 doi:10.1016/j.tecto.2012.03.005.
- 715 Kumar, P., Kawakatsu, H., Shinohara, M., Kanazawa, T., Araki, E., Suyehiro, K., 2011. P and S receiver function analysis of seafloor borehole  
716 broadband seismic data. *Journal of Geophysical Research: Solid Earth* 116. doi:10.1029/2011jb008506.
- 717 Langston, C.A., 1979. Structure under Mount Rainier, Washington, inferred from teleseismic body waves. *Journal of Geophysical Research: Solid*  
718 *Earth* 84, 4749–4762. doi:10.1029/jb084ib09p04749.
- 719 Leven, J., 1985. The application of synthetic seismograms to the interpretation of the upper mantle P-wave velocity structure in northern Australia.  
720 *Physics of the Earth and Planetary Interiors* 38, 9–27. doi:10.1016/0031-9201(85)90119-0.
- 721 Levin, V., Park, J., 1997. P-SH conversions in a flat-layered medium with anisotropy of arbitrary orientation. *Geophysical Journal International*  
722 131, 253–266. doi:10.1111/j.1365-246x.1997.tb01220.x.
- 723 Liu, L., Tong, S., Li, S., Qaysi, S., 2020. Sp Receiver-Function Images of African and Arabian Lithosphere: Survey of Newly Available Broadband  
724 Data. *Seismological Research Letters* 91, 1813–1819. doi:10.1785/0220190311.
- 725 Magrini, F., Kästle, E., Pilia, S., Rawlinson, N., Siena, L., 2023. A New Shear-Velocity Model of Continental Australia Based on Multi-Scale  
726 Surface-Wave Tomography. *Journal of Geophysical Research: Solid Earth* 128. doi:10.1029/2023jb026688.
- 727 Metropolis, N., Rosenbluth, A.W., Rosenbluth, M.N., Teller, A.H., Teller, E., 1953. Equation of State Calculations by Fast Computing Machines.  
728 *The Journal of Chemical Physics* 21, 1087–1092. doi:10.1063/1.1699114.
- 729 Myers, J.S., Shaw, R.D., Tyler, I.M., 1996. Tectonic evolution of Proterozoic Australia. *Tectonics* 15, 1431–1446. doi:10.1029/96tc02356.

## Lateral changes in the upper mantle discontinuities

- 730 Nagaya, M., Oda, H., Akazawa, H., Ishise, M., 2008. Receiver Functions of Seismic Waves in Layered Anisotropic Media: Application to the  
731 Estimate of Seismic Anisotropy Receiver Functions of Seismic Waves in Layered Anisotropic Media. *Bulletin of the Seismological Society of*  
732 *America* 98, 2990–3006. doi:10.1785/0120080130.
- 733 Nagaya, M., Oda, H., Kamimoto, T., 2011. Regional variation in shear-wave polarization anisotropy of the crust in southwest Japan as estimated by  
734 splitting analysis of Ps-converted waves on receiver functions. *Physics of the Earth and Planetary Interiors* 187, 56–65. doi:10.1016/j.pepi.  
735 2011.04.016.
- 736 Nataf, H.C., Ricard, Y., 1996. 3SMAC: an a priori tomographic model of the upper mantle based on geophysical modeling. *Physics of the Earth*  
737 *and Planetary Interiors* 95, 101–122. doi:10.1016/0031-9201(95)03105-7.
- 738 Office, M., 2010. Cartopy: a cartographic python library with a Matplotlib interface URL: <https://scitools.org.uk/cartopy>.
- 739 Park, J., Levin, V., 2016. Anisotropic shear zones revealed by backazimuthal harmonics of teleseismic receiver functions. *Geophysical Journal*  
740 *International* 207, 1216–1243. doi:10.1093/gji/ggw323.
- 741 Plomerová, J., Kouba, D., Babuška, V., 2002. Mapping the lithosphere–asthenosphere boundary through changes in surface-wave anisotropy.  
742 *Tectonophysics* 358, 175–185. doi:10.1016/s0040-1951(02)00423-7.
- 743 Pugh, S., Jenkins, J., Boyce, A., Cottaar, S., 2021. Global receiver function observations of the X-discontinuity reveal recycled basalt beneath  
744 hotspots. *Earth and Planetary Science Letters* 561, 116813. doi:10.1016/j.epsl.2021.116813.
- 745 Rein, T., Hannemann, K., Thomas, C., Korn, M., 2020. Location and characteristics of the X-discontinuity beneath SW Morocco and the adjacent  
746 shelf area using P-wave receiver functions. *Geophysical Journal International* 223, 1780–1793. doi:10.1093/gji/ggaa379.
- 747 Revenaugh, J., Jordan, T.H., 1991. Mantle layering from ScS reverberations: 3. The upper mantle. *Journal of Geophysical Research: Solid Earth*  
748 96, 19781–19810. doi:10.1029/91jb01487.
- 749 Rychert, C.A., Fischer, K.M., Rondenay, S., 2005. A sharp lithosphere–asthenosphere boundary imaged beneath eastern North America. *Nature*  
750 436, 542–545. doi:10.1038/nature03904.
- 751 Rychert, C.A., Rondenay, S., Fischer, K.M., 2007. P-to-S and S-to-P imaging of a sharp lithosphere–asthenosphere boundary beneath eastern North  
752 America. *Journal of Geophysical Research: Solid Earth* (1978–2012) 112. doi:10.1029/2006jb004619.
- 753 Saito, M., 1988. DISPER80 : A subroutine package for the calculation of seismic normal mode solutions, *Seismological Algorithms*, p. 293–319.
- 754 Salmon, M., Kennett, B.L.N., Saygin, E., 2013. Australian Seismological Reference Model (AuSREM): crustal component. *Geophysical Journal*  
755 *International* 192, 190–206. doi:10.1093/gji/ggs004.
- 756 Sambridge, M., 2014. A Parallel Tempering algorithm for probabilistic sampling and multimodal optimization. *Geophysical Journal International*  
757 196, 357–374. doi:10.1093/gji/ggt342.
- 758 Selway, K., Ford, H., Kelemen, P., 2015. The seismic mid-lithosphere discontinuity. *Earth and Planetary Science Letters* 414, 45–57.  
759 doi:10.1016/j.epsl.2014.12.029.
- 760 Shi, D., Wu, Z., Klemperer, S.L., Zhao, W., Xue, G., Su, H., 2015. Receiver function imaging of crustal suture, steep subduction, and mantle wedge  
761 in the eastern India–Tibet continental collision zone. *Earth and Planetary Science Letters* 414, 6–15. doi:10.1016/j.epsl.2014.12.055.
- 762 Shibutani, T., Ueno, T., Hirahara, K., 2008. Improvement in the Extended-Time Multitaper Receiver Function Estimation Technique Short Note.  
763 *Bulletin of the Seismological Society of America* 98, 812–816. doi:10.1785/0120070226.
- 764 Shiomi, K., Park, J., 2008. Structural features of the subducting slab beneath the Kii Peninsula, central Japan: Seismic evidence of slab segmentation,  
765 dehydration, and anisotropy. *Journal of Geophysical Research: Solid Earth* 113. doi:10.1029/2007jb005535.
- 766 Simons, F.J., Hilst, R.D.V.D., Montagner, J., Zielhuis, A., 2002. Multimode Rayleigh wave inversion for heterogeneity and azimuthal anisotropy of  
767 the Australian upper mantle. *Geophysical Journal International* 151, 738–754. doi:10.1046/j.1365-246x.2002.01787.x.

- 768 Sippl, C., 2016. Moho geometry along a north–south passive seismic transect through Central Australia. *Tectonophysics* 676, 56–69. doi:10.  
769 1016/j.tecto.2016.03.031.
- 770 Srinu, U., Kumar, P., Haldar, C., Kumar, M.R., Srinagesh, D., Illa, B., 2021. X-Discontinuity Beneath the Indian Shield—Evidence for Remnant  
771 Tethyan Oceanic Lithosphere in the Mantle. *Journal of Geophysical Research: Solid Earth* 126. doi:10.1029/2021jb021890.
- 772 Sun, W., Fu, L., Saygin, E., Zhao, L., 2018. Insights Into Layering in the Cratonic Lithosphere Beneath Western Australia. *Journal of Geophysical*  
773 *Research: Solid Earth* 123, 1405–1418. doi:10.1002/2017jb014904.
- 774 Taira, T., Yoshizawa, K., 2020. Upper-mantle discontinuities beneath Australia from transdimensional Bayesian inversions using multimode  
775 surface waves and receiver functions. *Geophysical Journal International* 223, 2085–2100. URL: <https://doi.org/10.1093/gji/ggaa442>,  
776 doi:10.1093/gji/ggaa442.
- 777 Takagi, R., Nishida, K., 2022. Multimode dispersion measurement of surface waves extracted by multicomponent ambient noise cross-correlation  
778 functions. *Geophysical Journal International* 231, 1196–1220. doi:10.1093/gji/ggac225.
- 779 TAKEUCHI, H., SAITO, M., 1972. Seismic Surface Waves. *Methods in Computational Physics: Advances in Research and Applications* 11,  
780 217–295. doi:10.1016/b978-0-12-460811-5.50010-6.
- 781 Tarumi, K., Yoshizawa, K., 2024. Numerical Sheet for "Station-orientation catalog for Australian broadband seismic stations". URL: <https://doi.org/10.5281/zenodo.13985090>.  
782 [//doi.org/10.5281/zenodo.13985090](https://doi.org/10.5281/zenodo.13985090).
- 783 Thomson, W.T., 1950. Transmission of Elastic Waves through a Stratified Solid Medium. *Journal of Applied Physics* 21, 89–93. doi:10.1063/1.  
784 1699629.
- 785 Thybo, H., 2006. The heterogeneous upper mantle low velocity zone. *Tectonophysics* 416, 53–79. doi:10.1016/j.tecto.2005.11.021.
- 786 Tkalčić, H., Chen, Y., Liu, R., Zhibin, H., Sun, L., Chan, W., 2011. Multistep modelling of teleseismic receiver functions combined with constraints  
787 from seismic tomography: crustal structure beneath southeast China. *Geophysical Journal International* 187, 303–326. doi:10.1111/j.  
788 1365-246x.2011.05132.x.
- 789 Tkalčić, H., Pasyanos, M.E., Rodgers, A.J., Gök, R., Walter, W.R., Al-Amri, A., 2006. A multistep approach for joint modeling of surface wave  
790 dispersion and teleseismic receiver functions: Implications for lithospheric structure of the Arabian Peninsula: MULTISTEP MODELING OF  
791 ARABIAN LITHOSPHERE. *Journal of Geophysical Research: Solid Earth* 111, n/a–n/a. doi:10.1029/2005jb004130.
- 792 Tonegawa, T., Hirahara, K., Shibutani, T., 2005. Detailed structure of the upper mantle discontinuities around the Japan subduction zone imaged  
793 by receiver function analyses. *Earth, Planets and Space* 57, 5–14. doi:10.1186/bf03351801.
- 794 Uieda, L., Tian, D., Leong, W.J., Jones, M., Schlitzer, W., Toney, L., Grund, M., Yao, J., Magen, Y., Materna, K., Newton, T., Anant, A., Ziebarth, M.,  
795 Wessel, P., Quinn, J., 2021. PyGMT: A Python interface for the Generic Mapping Tools URL: <https://doi.org/10.5281/zenodo.5607255>,  
796 doi:10.5281/zenodo.5607255. the development of PyGMT has been supported by NSF grants OCE-1558403 and EAR-1948603.
- 797 Vinnik, L., Kurnik, E., Farra, V., 2005. Lehmann discontinuity beneath North America: No role for seismic anisotropy. *Geophysical Research*  
798 *Letters* 32. doi:10.1029/2004gl022333.
- 799 Vinnik, L.P., Erduran, M., Oreshin, S.I., Kosarev, G.L., Kutlu, Y.A., Çakir, , Kiselev, S.G., 2014. Joint inversion of P- and S-receiver functions  
800 and dispersion curves of Rayleigh waves: The results for the Central Anatolian Plateau. *Izvestiya, Physics of the Solid Earth* 50, 622–631.  
801 doi:10.1134/s106935131404017x.
- 802 Wessel, P., Luis, J.F., Uieda, L., Scharroo, R., Wobbe, F., Smith, W.H.F., Tian, D., 2019. The Generic Mapping Tools Version 6. *Geochemistry,*  
803 *Geophysics, Geosystems* 20, 5556–5564. doi:10.1029/2019gc008515.
- 804 Xu, H., Beghein, C., 2019. Measuring higher mode surface wave dispersion using a transdimensional Bayesian approach. *Geophysical Journal*  
805 *International* 218, 333–353. doi:10.1093/gji/ggz133.

## Lateral changes in the upper mantle discontinuities

- 806 Xu, H., Beghein, C., Panning, M.P., Drilleau, M., Lognonné, P., Driel, M.v., Ceylan, S., Böse, M., Brinkman, N., Clinton, J., Euchner, F., Giardini,  
807 D., Horleston, A., Kawamura, T., Kenda, B., Murdoch, N., Stähler, S., 2021. Measuring Fundamental and Higher Mode Surface Wave Dispersion  
808 on Mars From Seismic Waveforms. *Earth and Space Science* 8. doi:10.1029/2020ea001263.
- 809 Yoshida, M., Yoshizawa, K., 2020. Continental Drift with Deep Cratonic Roots. *Annual Review of Earth and Planetary Sciences* 49, 1–23.  
810 doi:10.1146/annurev-earth-091620-113028.
- 811 Yoshizawa, K., 2014. Radially anisotropic 3-D shear wave structure of the Australian lithosphere and asthenosphere from multi-mode surface waves.  
812 *Physics of the Earth and Planetary Interiors* 235, 33–48. doi:10.1016/j.pepi.2014.07.008.
- 813 Yoshizawa, K., Ekström, G., 2010. Automated multimode phase speed measurements for high-resolution regional-scale tomography: application to  
814 North America. *Geophysical Journal International* 183, 1538–1558. doi:10.1111/j.1365-246x.2010.04814.x.
- 815 Yoshizawa, K., Kennett, B.L.N., 2002a. Determination of the influence zone for surface wave paths. *Geophysical Journal International* 149, 440–453.  
816 doi:10.1046/j.1365-246x.2002.01659.x.
- 817 Yoshizawa, K., Kennett, B.L.N., 2002b. Non-linear waveform inversion for surface waves with a neighbourhood algorithm—application to  
818 multimode dispersion measurements. *Geophysical Journal International* 149, 118–133. doi:10.1046/j.1365-246x.2002.01634.x.
- 819 Yoshizawa, K., Kennett, B.L.N., 2004. Multimode surface wave tomography for the Australian region using a three-stage approach incorporating  
820 finite frequency effects. *Journal of Geophysical Research: Solid Earth* 109. doi:10.1029/2002jb002254.
- 821 Yoshizawa, K., Kennett, B.L.N., 2015. The lithosphere-asthenosphere transition and radial anisotropy beneath the Australian continent. *Geophysical*  
822 *Research Letters* 42, 3839–3846. doi:10.1002/2015gl063845.
- 823 Yuan, H., Romanowicz, B., Fischer, K.M., Abt, D., 2011. 3-D shear wave radially and azimuthally anisotropic velocity model of the North American  
824 upper mantle. *Geophysical Journal International* 184, 1237–1260. doi:10.1111/j.1365-246x.2010.04901.x.

## Supplementary Material for

# Detecting rapid lateral changes of upper mantle discontinuities using azimuth-dependent P-wave receiver functions and multimode surface waves

5

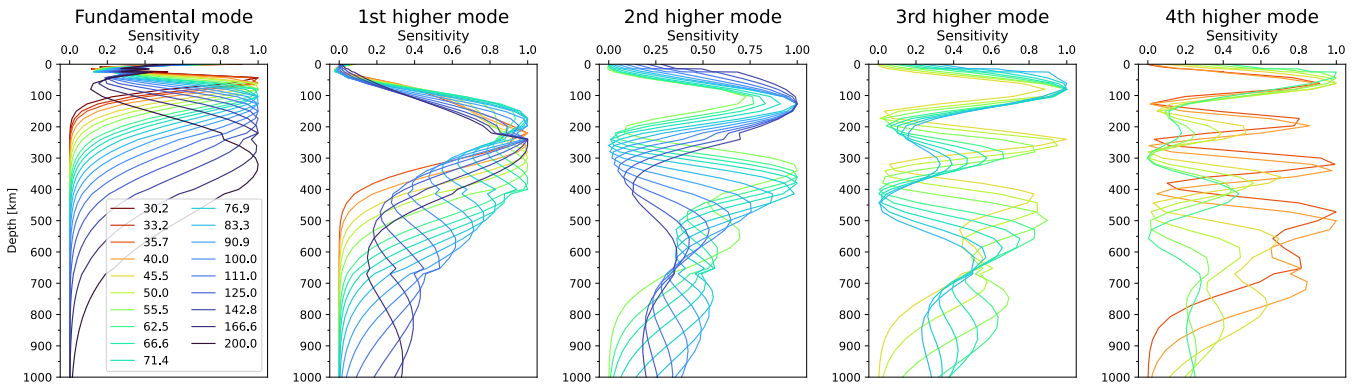
K. Tarumi<sup>1,\*</sup> and K. Yoshizawa<sup>1,2</sup>

<sup>1</sup> Department of Natural History Sciences, Graduate School of Science, Hokkaido University, Sapporo 060-0810, Japan

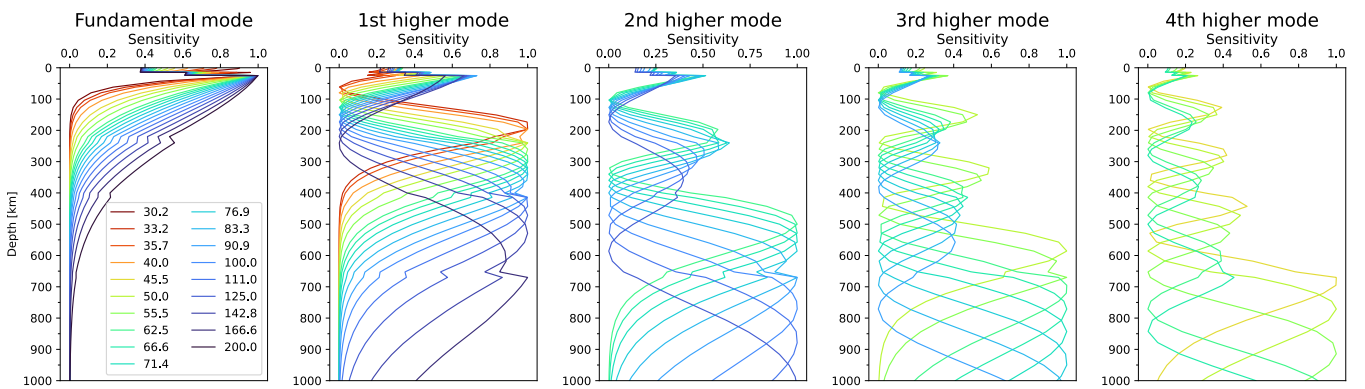
10 <sup>2</sup>Department of Earth & Planetary Sciences, Faculty of Science, Hokkaido University, Sapporo 060-0810, Japan.

\*Corresponding author: tarumi.kotaro.jp@gmail.com

(a) Rayleigh wave



(b) Love wave



15 Figure S1. Normalized sensitivity kernels of surface waves for anisotropic PREM (Dziewonski and Anderson, 1981) from the fundamental to the 4th higher mode of (a) Rayleigh waves and (b) Love waves. Line colors indicate the period of surface waves.

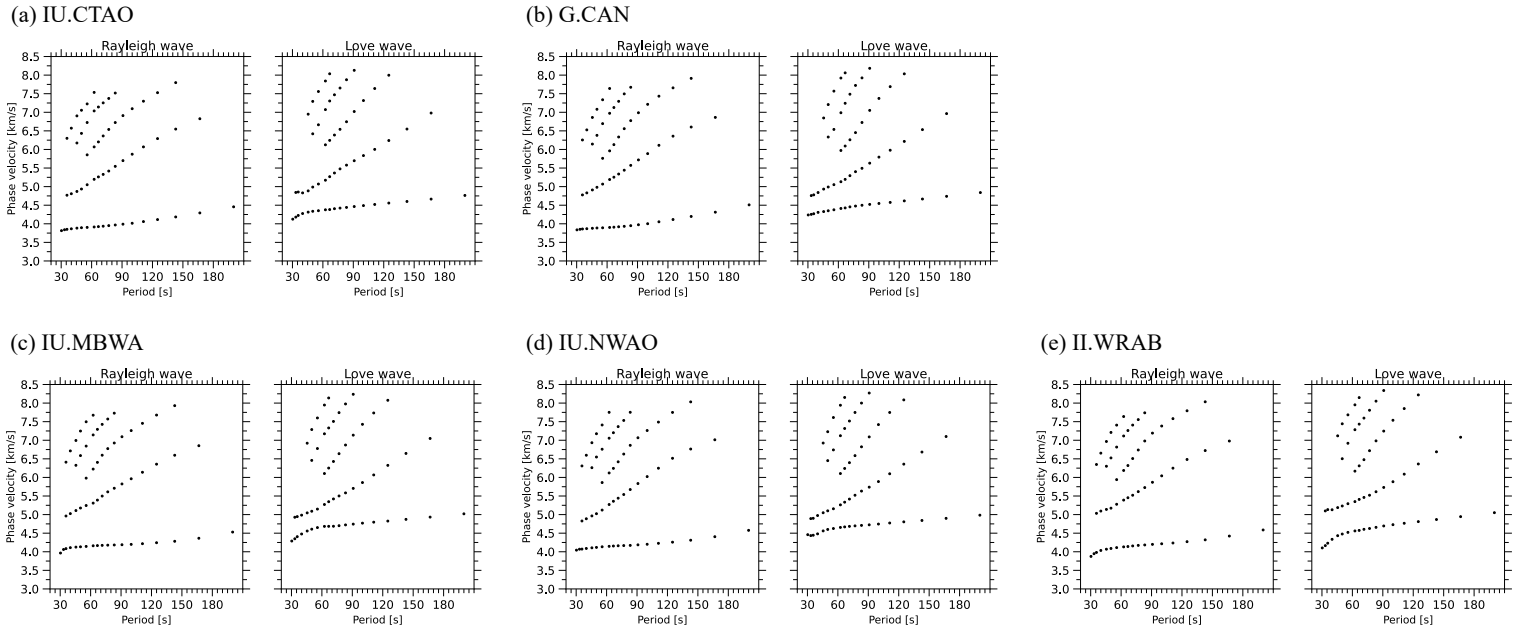


Figure S2: Phase speed dispersion data of multimode Rayleigh and Love waves for five

stations used in this study (a: IU.CTAO; b: G.CAN; c: IU.MBWA; d: IU.NWAO; e:

20 II.WRAB). These dispersion data are extracted from multimode phase velocity maps by

Yoshizawa (2014).

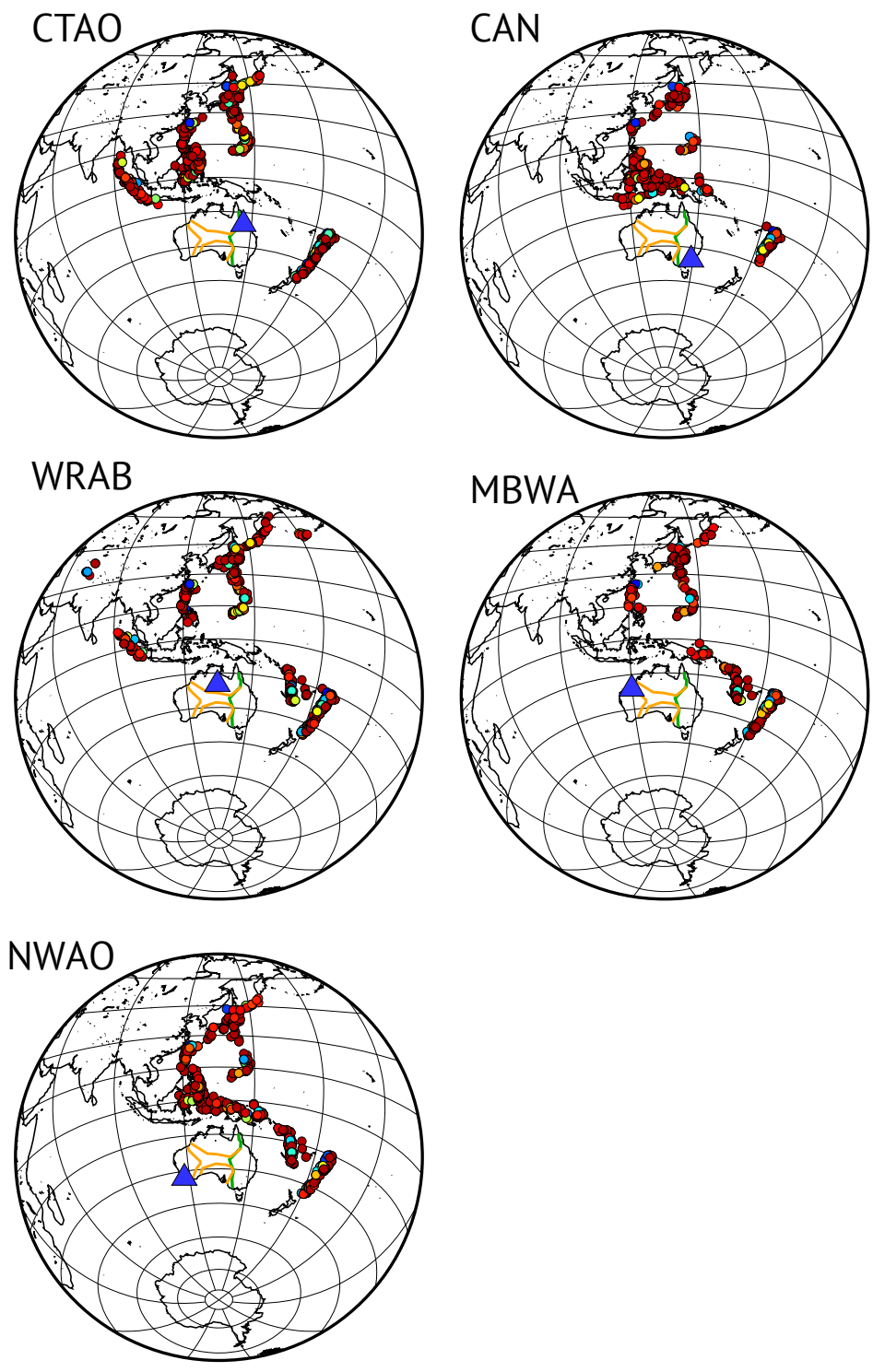
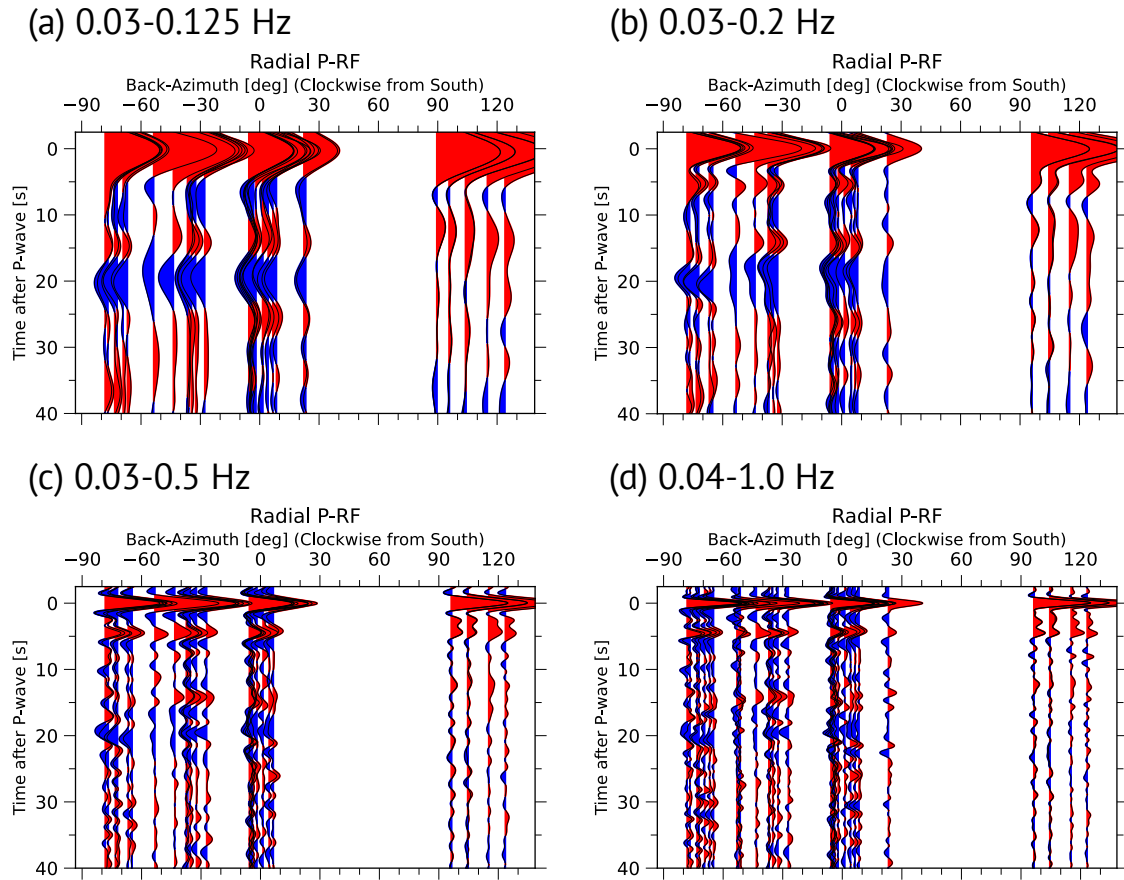


Figure S3: Event distributions for each station used in this study. Notations are the same as Figure 3 (e).



25

Figure S4: Frequency-dependent P-wave receiver functions (P-RFs) at IU.CTAO for four frequency ranges: (a) 0.03-0.125 Hz, (b) 0.03-0.2 Hz, (c) 0.03-0.5 Hz, and (d) 0.04-1.0 Hz. Red and blue colors represent the positive and negative phases in receiver functions.

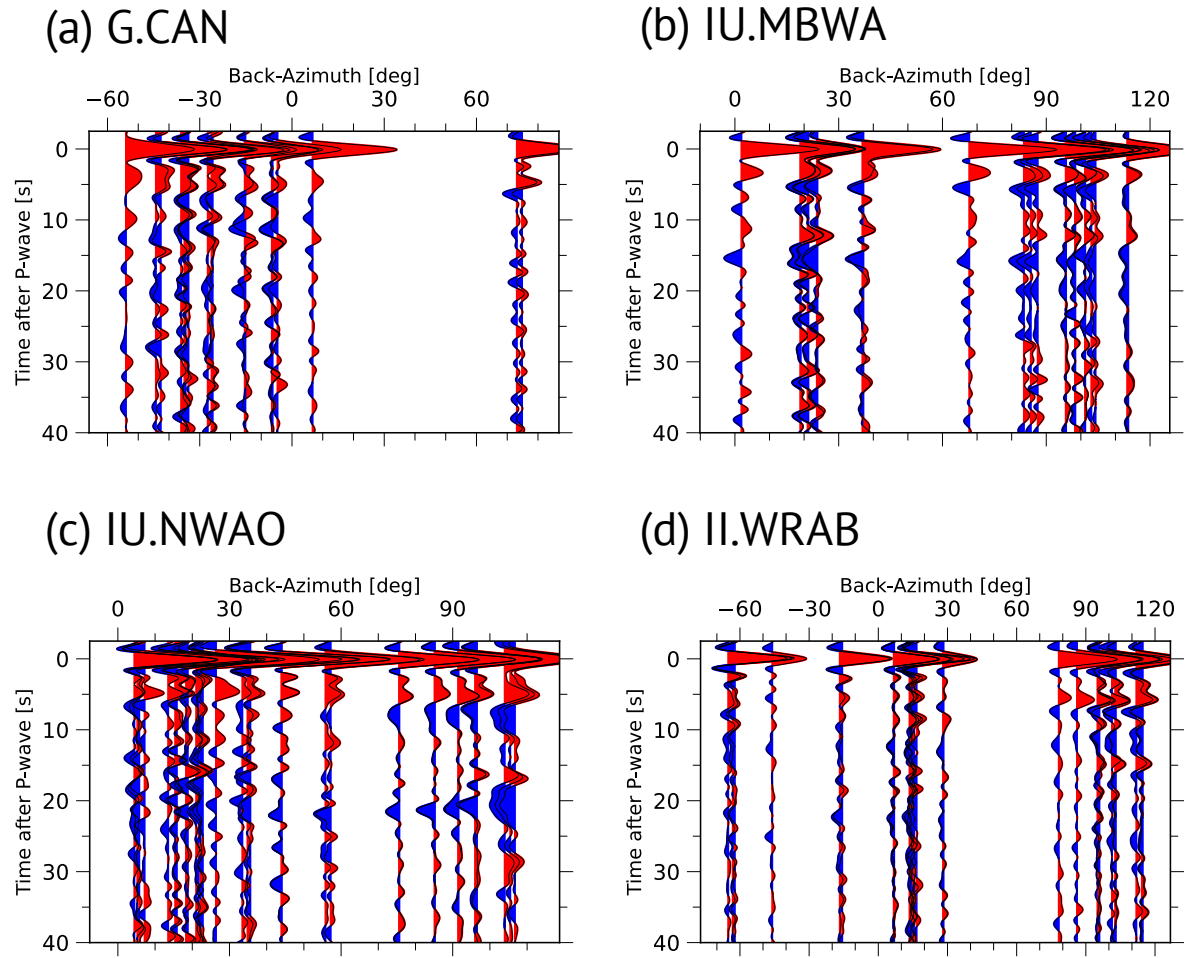
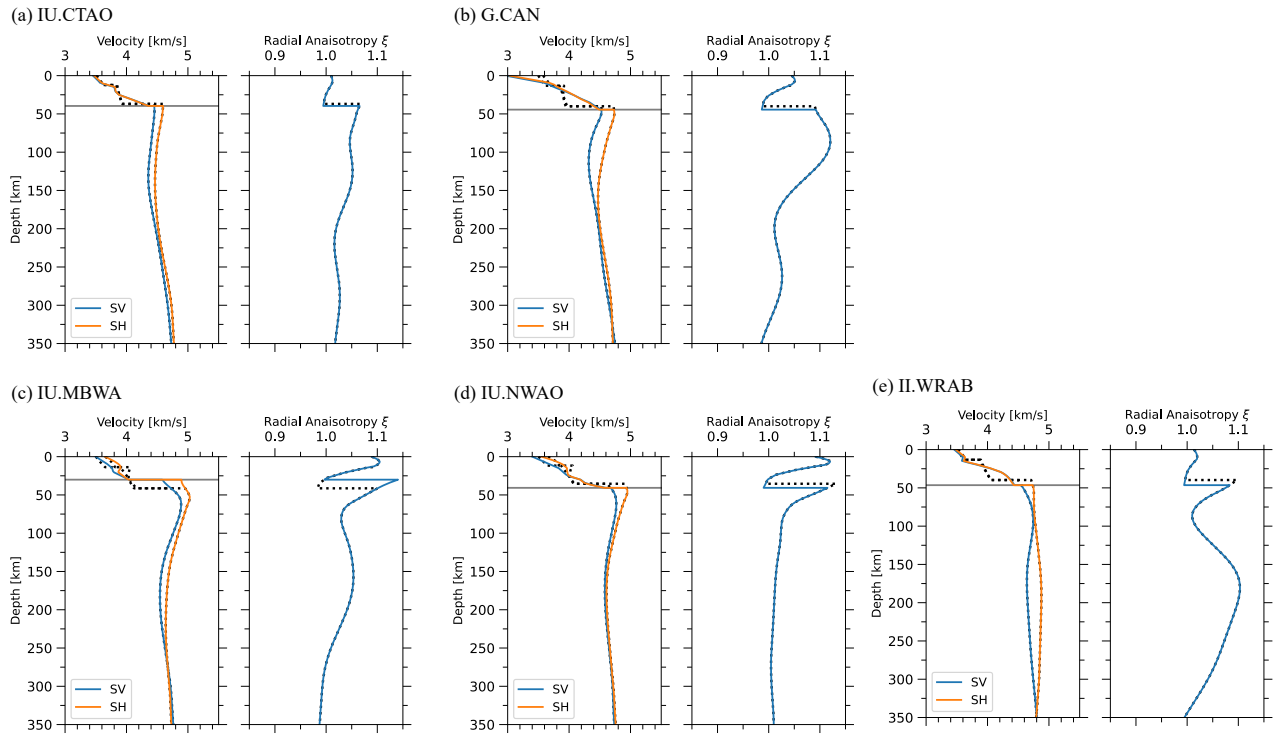
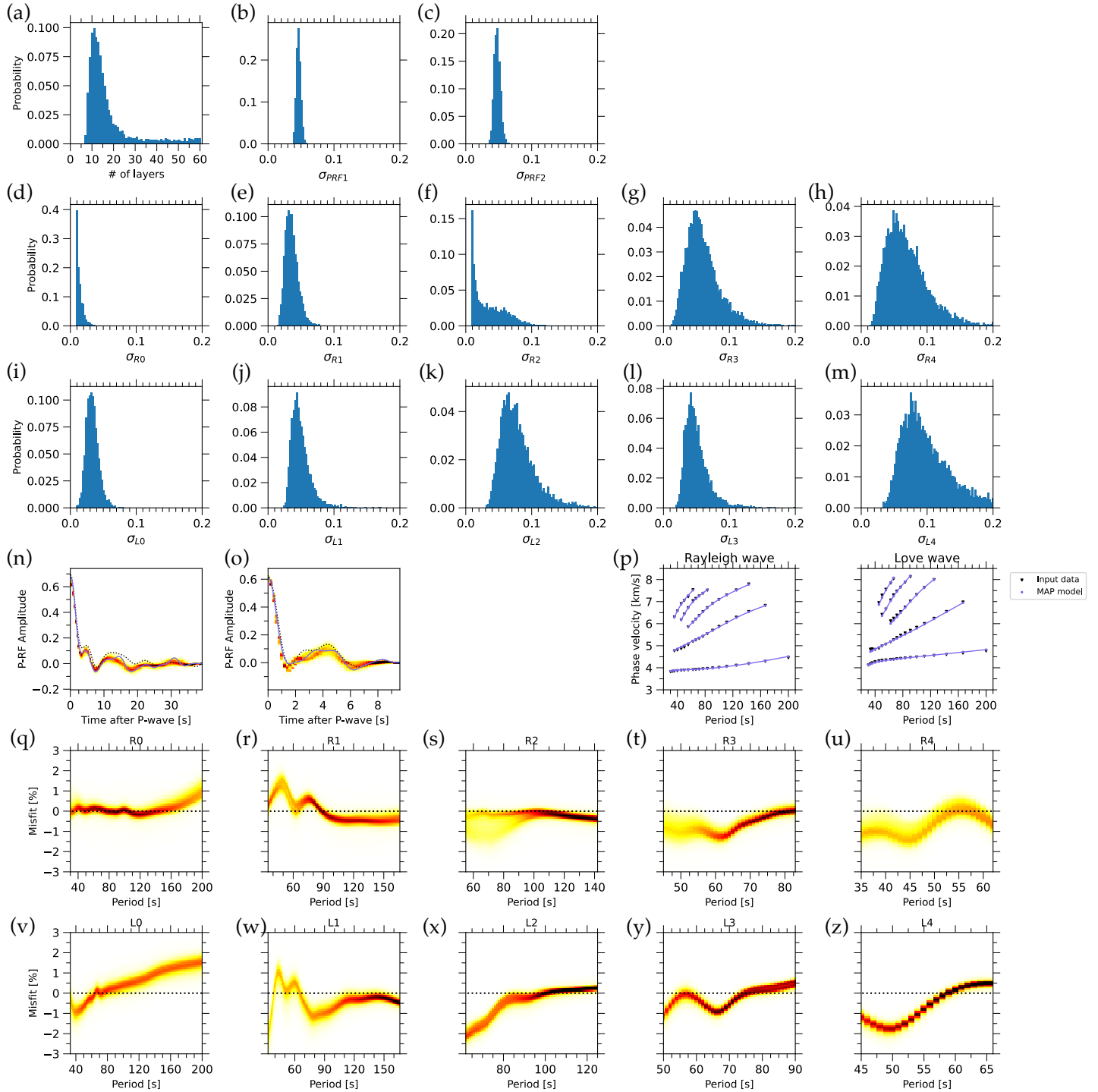


Figure S5: Same as Figure 3 in the main text, but for 0.03-0.5 Hz.

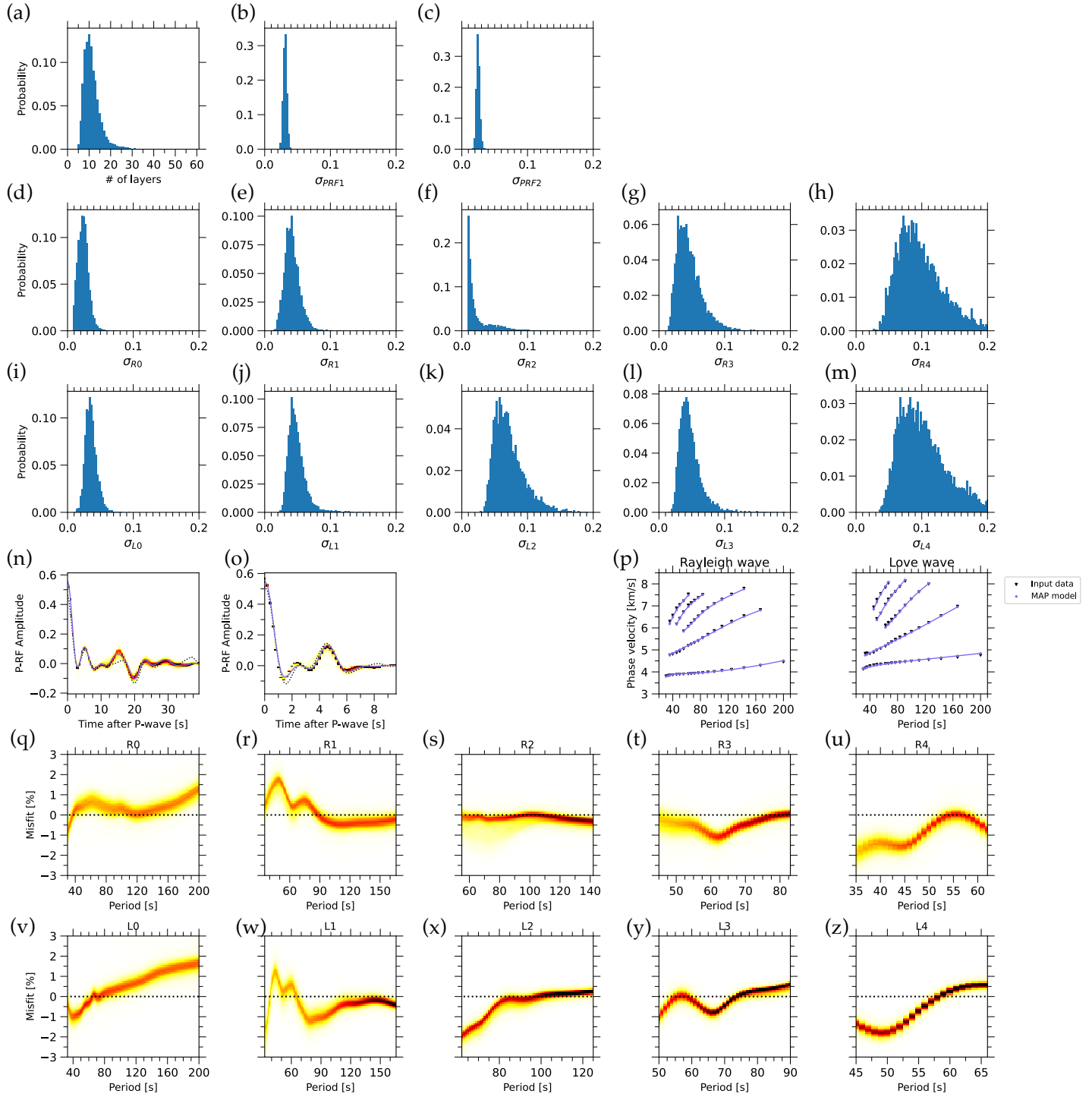


30 Figure S6: Local reference structural models (SV and SH velocities and radial anisotropy) for each station. Solid colored lines represent the reference SV and SH wave models used in this study taken from the 3-D radially anisotropic tomographic model (Yoshizawa, 2014), replacing the crust with AuSREM (Kennett *et al.*, 2013; Salmon, Kennett and Saygin, 2013) and AusMoho (Kennett *et al.*, 2011, 2023).



35 Figure S7: Posterior distributions of hyperparameters and marginal distributions of data misfit for IU.CTAO results using the eastern event group (Figure 5 (b)). (a) The number of layers. (b, c) Data noises for the low-frequency P-RF ( $\sigma_{PRF1}$ ) and the high-frequency P-RF

( $\sigma_{PRF2}$ ). Data noises for each mode of (d-h) Rayleigh waves (d-h) and (i-m) Love wave. R0 and L0 indicate the fundamental-mode Rayleigh and Love waves, and Rx and Lx  
40 (1≤x≤4) represent their overtones. (n, o) Marginal posteriors of misfit distribution of (n) low- and (o) high-frequency P-RFs. Black dotted lines and purple solid lines indicate the objective data to be fitted in the inversion process and best-fitted P-RF traces. (p) The best-fitted dispersion curves for Rayleigh and Love waves. Purple lines and dots represent the best-fit synthetic data. Black inverse triangles show the dispersion data from phase speed  
45 maps (Yoshizawa, 2014). Marginal misfit distributions between the objective and predicted dispersion curves for (q-u) Rayleigh and (v-z) Love waves. The misfit values are shown in the form of fractional perturbation,  $\frac{c_{pre}-c_{obs}}{c_{pre}} \times 100$ , following Taira and Yoshizawa (2020). Notations of Rx and Lx are the same as (d-m). Black dotted lines represent the zero-misfit.



50 Figure S8: Same as Figure S7, but for the western event group (Figure 5 (c) in the main text).

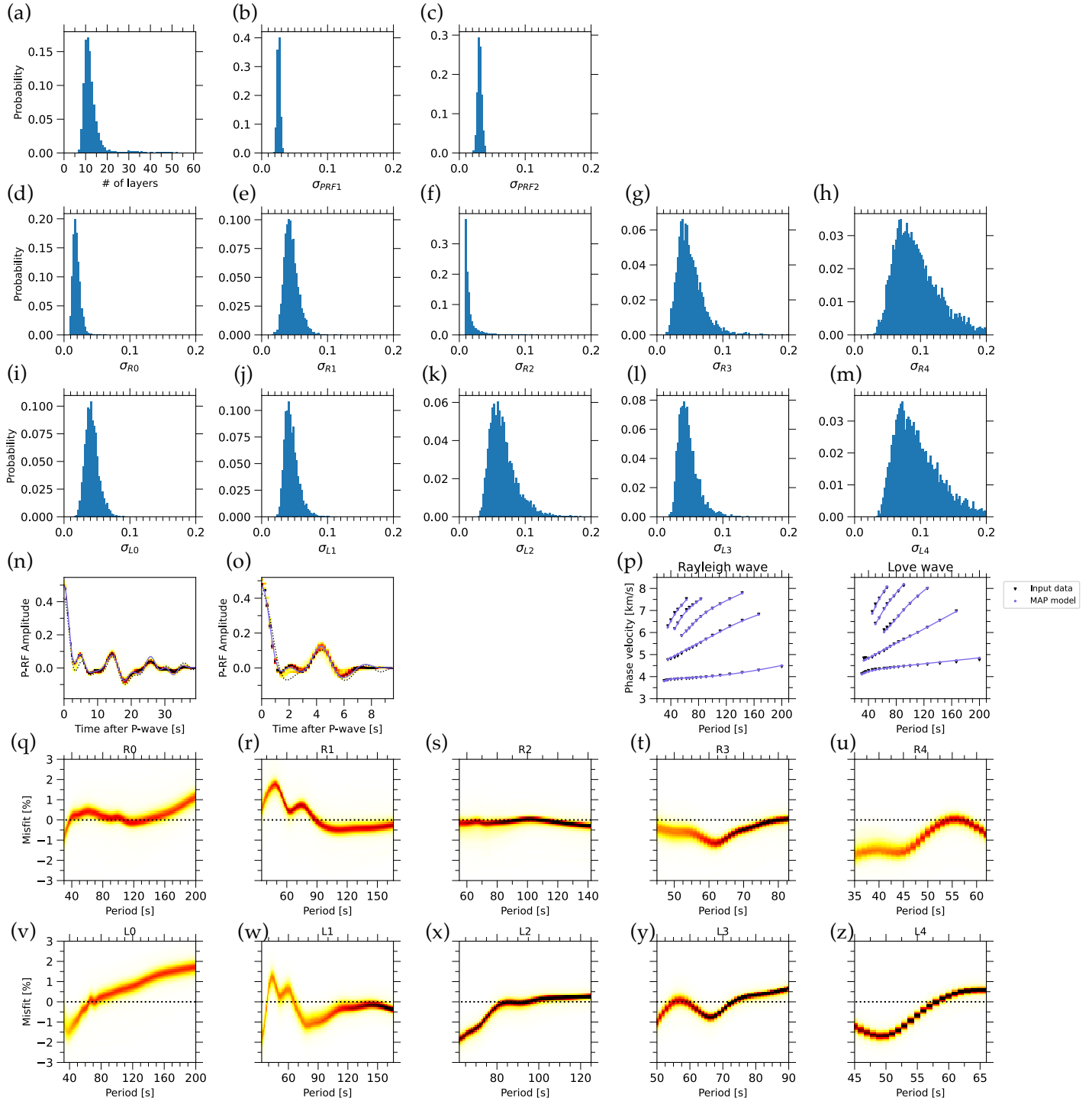


Figure S9: Same as Figure S7, but for the northern event group (Figure 5 (d) in the main text).

Dziewonski, A.M. and Anderson, D.L. (1981) "Preliminary reference Earth model," *Physics of the Earth and Planetary Interiors*, 25(4), pp. 297–356. Available at: [https://doi.org/10.1016/0031-9201\(81\)90046-7](https://doi.org/10.1016/0031-9201(81)90046-7).

60 Kennett, B.L.N. *et al.* (2011) "AusMoho: the variation of Moho depth in Australia," *Geophysical Journal International*, 187(2), pp. 946–958. Available at: <https://doi.org/10.1111/j.1365-246x.2011.05194.x>.

Kennett, B.L.N. *et al.* (2013) "Australian Seismological Reference Model (AuSREM): mantle component," *Geophysical Journal International*, 192(2), pp. 871–887. Available at: <https://doi.org/10.1093/gji/ggs065>.

65 Kennett, B.L.N. *et al.* (2023) "Refining the Moho across the Australian continent," *Geophysical Journal International*, 233(3), pp. 1863–1877. Available at: <https://doi.org/10.1093/gji/ggad035>.

Salmon, M., Kennett, B.L.N. and Saygin, E. (2013) "Australian Seismological Reference Model (AuSREM): crustal component," *Geophysical Journal International*, 192(1), pp. 190–206. Available at: <https://doi.org/10.1093/gji/ggs004>.

Taira, T. and Yoshizawa, K. (2020) "Upper–mantle discontinuities beneath Australia from transdimensional Bayesian inversions using multimode surface waves and receiver functions," *Geophysical Journal International*, 223(3), pp. 2085–2100. Available at: <https://doi.org/10.1093/gji/ggaa442>.

75 Yoshizawa, K. (2014) "Radially anisotropic 3–D shear wave structure of the Australian lithosphere and asthenosphere from multi–mode surface waves," *Physics of the Earth and Planetary Interiors*, 235, pp. 33–48. Available at: <https://doi.org/10.1016/j.pepi.2014.07.008>.

